Supporting Information

Investigating State Restriction in Fluorescent Protein FRET Using Time-Resolved Fluorescence and Anisotropy

Thomas S. Blacker[1,2,3], WeiYue Chen[4], Edward Avezov[5], Richard J. Marsh[1,†], Michael R. Duchen[3], Clemens F. Kaminski[4], Angus J. Bain[1,2,*]

[1]Department of Physics & Astronomy, University College London, Gower Street, London, WC1E 6BT, United Kingdom

[2]Centre for Mathematics and Physics in the Life Sciences and Experimental Biology, University College London, Gower Street, London, WC1E 6BT, United Kingdom

[3]Department of Cell & Developmental Biology, University College London, Gower Street, London, WC1E 6BT, United Kingdom

[4]Department of Chemical Engineering and Biotechnology, University of Cambridge, Pembroke Street, Cambridge, CB2 3RA, United Kingdom

[5]Cambridge Institute for Medical Research, University of Cambridge, Cambridge, CB2 0XY, United Kingdom

[†]Current Address: Cancer Cell Biology & Imaging, King's College London, New Hunt's House, Newcomen Street, London, SE1 1UL, United Kingdom

*Corresponding Author: a.bain@ucl.ac.uk

Appendix S1: Donor and Acceptor Window Selection

Emission spectra of OG and mC were obtained from the manufacturers (ThermoFisher Scientific Fluorescence SpectraViewer) and literature[1] respectively and are shown in Figure S1A. The donor and acceptor fluorescence windows were created using 515 nm long pass and 540 nm short pass filters and 630 nm long pass filter and 650 nm short pass filters (all Newport, UK). The wavelength transmission curves of these filter sets were obtained by measuring their spectral absorption of a xenon white light source using a UV-VIS USB spectrometer (USB4000, Ocean Optics, UK), shown in Figure S1B. Combining these datasets with the spectral efficiency of the PMT, the fractions of total donor and acceptor fluorescence detected in the donor window were calculated as $q_{\mathrm{D}}(\Delta\lambda_{\mathrm{D}})$ = 2.52% and $q_{\mathrm{A}}(\Delta\lambda_{\mathrm{D}})$ = 0.006% respectively. In the acceptor window, these values were $q_{\mathrm{D}}(\Delta\lambda_{\mathrm{A}})$ = 0.03% and $q_{\mathrm{A}}(\Delta\lambda_{\mathrm{A}})$ = 0.45%. The quantum yields of OG and mC are 0.91 and 0.22 respectively[1–3]. The parameter $B(\Delta\lambda)$ takes account of this difference in the intrinsic brightness of the donor and acceptor, quantifying the proportion of acceptor fluorescence detected relative to the donor over a given detection wavelength range $\Delta\lambda$ [4],

$$B(\Delta\lambda) = \frac{k_{\mathrm{rad}}^{\mathrm{A}} q_{\mathrm{A}}(\Delta\lambda)}{k_{\mathrm{rad}}^{\mathrm{D}} q_{\mathrm{D}}(\Delta\lambda)} \tag{S1}$$

where $k_{\mathrm{rad}}^{\mathrm{D}}$ and $k_{\mathrm{rad}}^{\mathrm{A}}$ are the radiative decay rates of the donor and acceptor. In an ideal donor window, $B(\Delta\lambda_{\mathrm{D}}) \approx 0$, indicating only donor fluorescence is observed. In an acceptor window where there is minimal donor bleed through, $B(\Delta\lambda_{\mathrm{A}})$ would be large. Moving to longer detector window wavelengths to minimize non-interacting donor bleed through reduces $q_{\mathrm{D}}(\Delta\lambda_{\mathrm{A}})$ but also reduces $q_{\mathrm{A}}(\Delta\lambda_{\mathrm{A}})$, leading to lower acceptor emission signals. Using the measurements of the fluorescence lifetimes of the two probes performed in this work, $B(\Delta\lambda_{\mathrm{A}})$ and $B(\Delta\lambda_{\mathrm{D}})$ values of 0.0017 and 9.7 were obtained. The presence of acceptor fluorescence could therefore be neglected in the donor window. However, donor bleed through into the acceptor window was more significant. The spectral overlap of the OG to mC FRET pair $O(\lambda)$, shown in Figure S2, was calculated from published spectra[1].

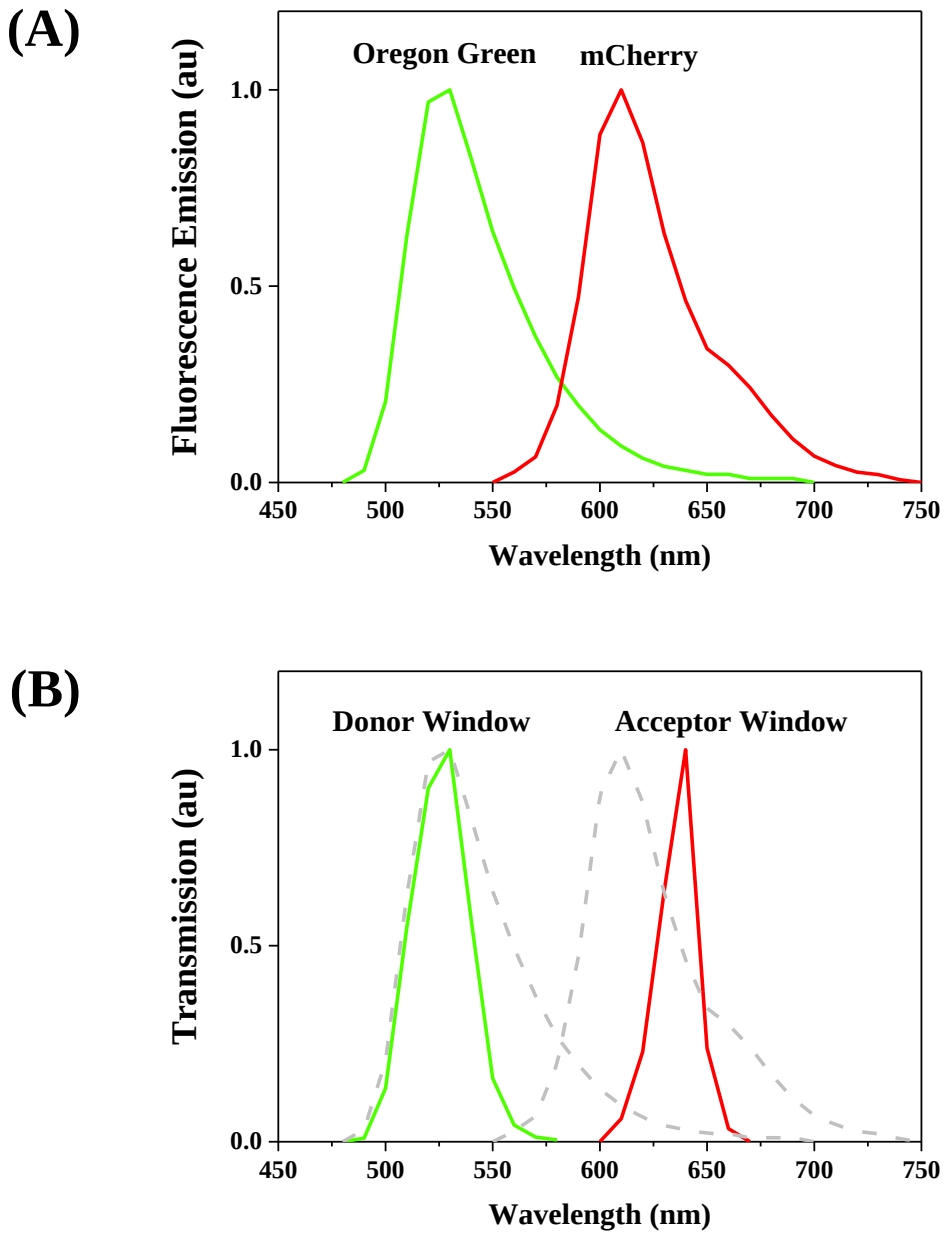

Figure S1: (A) Emission spectra of Oregon Green 488 and mCherry, provided by manufacturer and taken from Shaner et al.[1] respectively. These datasets were used to select filters to construct donor and acceptor emission windows, the transmission spectra of which are shown in (B).

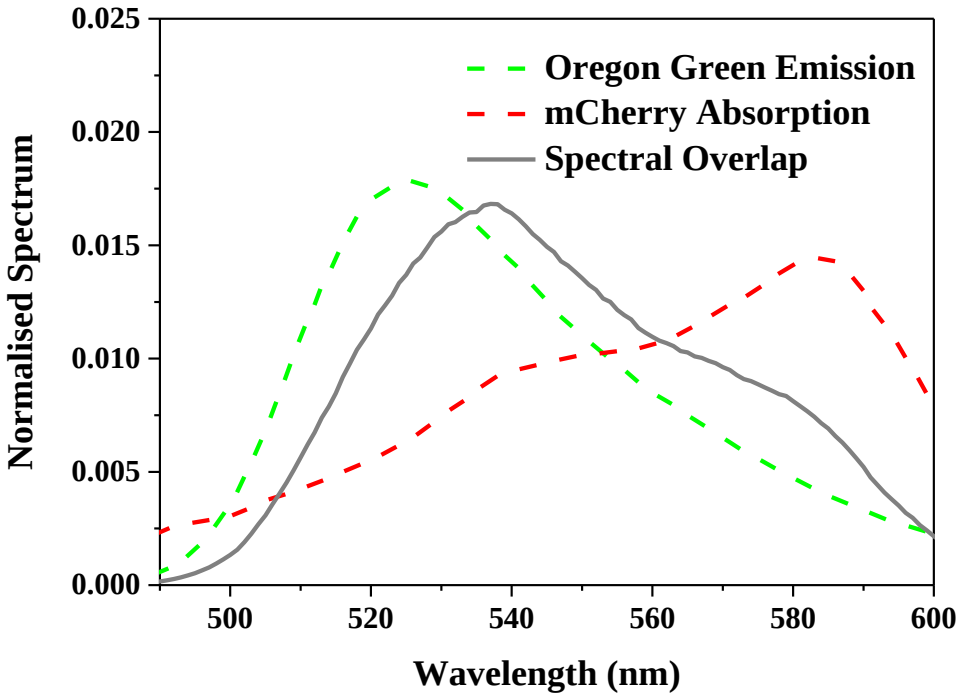

Figure S2: Normalised spectral overlap of the Oregon Green 488 and mCherry FRET pair, calculated by multiplying the OG488 emission spectrum, obtained from the manufacturer, with the mCherry absorption spectrum, obtained from Shaner et al.[1].

Appendix S2: Excitation wavelength selection

The two-photon absorption cross section spectrum of OG was measured in order to determine the optimum wavelength for donor excitation. Using a standard approach[5], the time-averaged two-photon fluorescence count rates $\langle I_{OG} \rangle$ were compared to those of an equimolar solution of the two-photon standard rhodamine B (RB) $\langle I_{RB} \rangle$ for excitation wavelengths ranging from 750 nm to 900 nm. A 700 nm short pass emission filter was used to prevent laser break-through. The OG two-photon absorption cross section at each excitation wavelength $\sigma_{OG}^{(2)}(\lambda_{ex})$ was then calculated from the ratio [5],

$$\sigma_{OG}^{(2)}(\lambda_{ex}) = \sigma_{RB}^{(2)}(\lambda_{ex}) \frac{q_{RB}(\Delta\lambda_{det})\phi_{RB}\langle I_{OG} \rangle}{q_{OG}(\Delta\lambda_{det})\phi_{OG}\langle I_{RB} \rangle} \quad \text{(S2)}$$

where $q_{OG}(\Delta\lambda_{det})$ and $q_{RB}(\Delta\lambda_{det})$ are the fractions of the total emission spectra of OG and RB that are that are detected, taking into account emission filtering and the wavelength-dependent efficiency of the PMT. ϕ_{RB} and ϕ_{OG} are the fluorescence quantum yields of the dyes (0.50 and 0.91 respectively [2,3,6]). The RB two-photon absorption cross-sections $\sigma_{RB}^{(2)}$ were obtained from the online Developmental Resource for Biophysical Imaging Optoelectronics (DRBIO), Cornell University[5]. The OG two-photon cross section values obtained in this experiment were combined with the equivalent data for mC, obtained from the literature[7] and shown in Figure S3A, to calculate $\delta(\lambda_{ex})$ (Figure S3B) which has a minimum value at 880nm of 6×10^{-3}. As such, direct acceptor excitation could be neglected at this excitation wavelength.

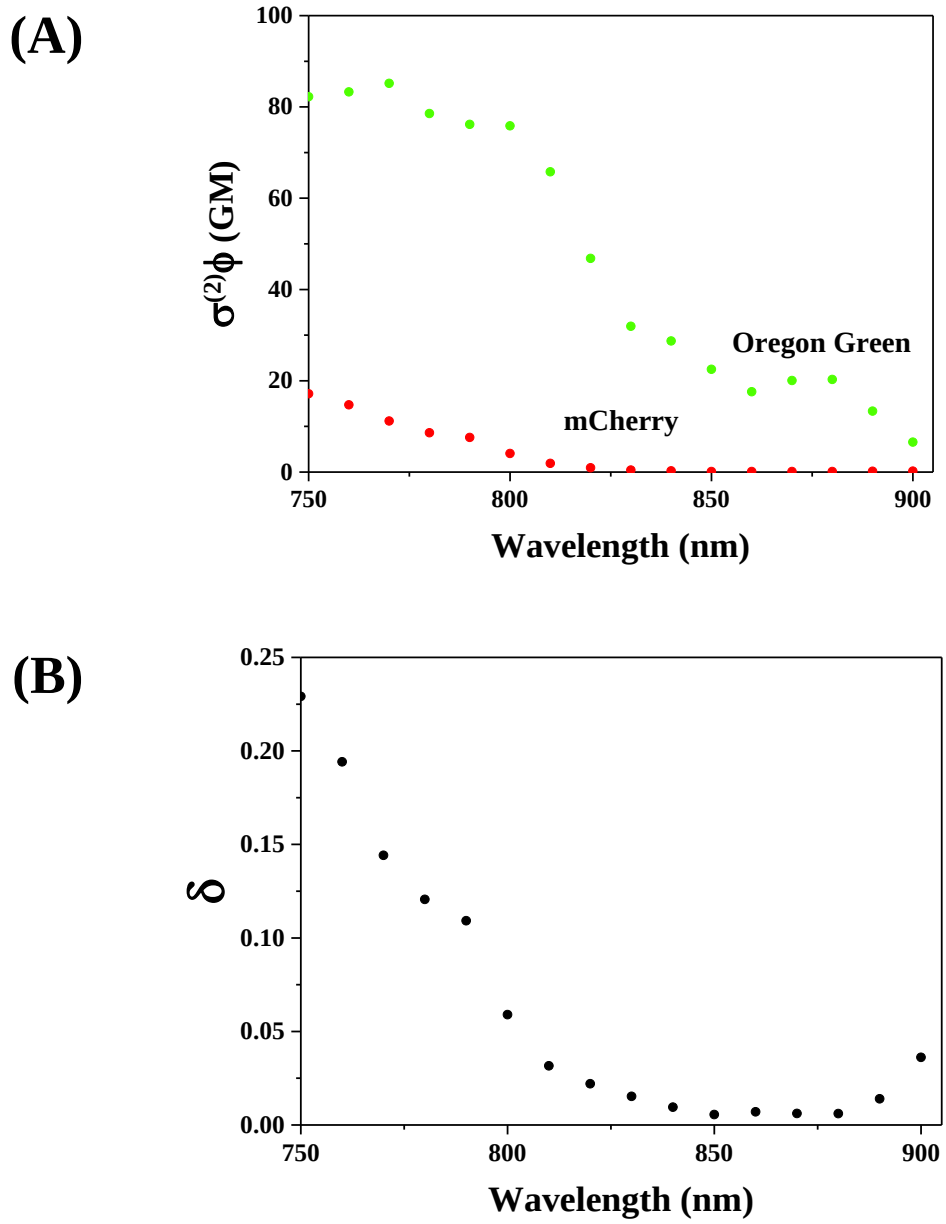

Figure S3: (A) Two-photon action cross sections ($\sigma^{(2)}\phi$) of Oregon Green 488, measured by quantitative comparison of fluorescence intensity with rhodamine B, and mCherry, obtained from Drobizhev et al.[8]. (B) The ratio of mCherry to OG absorption at each wavelength defines $\delta(\lambda)$, showing direct acceptor excitation is minimised at around $\lambda = 880$ nm.

Appendix S3: TCSPC Apparatus

Single-photon excitation was provided using the vertically polarised ~250 fs, 250 kHz pulses output by a tunable optical parametric amplifier (OPA 9400, Coherent, UK) pumped by a regeneratively amplified Ti:Sapphire laser (Mira900F, Coherent, UK) operating at 800 nm. This, in turn, was pumped by the 532 nm output of an Nd:YVO_4 laser (Verdi V18, Coherent, UK). Two-photon excitation was performed using the 76 MHz tunable output of the Ti:Sapphire directly, pulse-picked to 3.8 MHz (pulseSelect, APE, Germany).

Following excitation in a 5 mm path length quartz cuvette (Hellma, UK), fluorescence was collected with a 5 cm focal length lens in a 90° excitation–detection geometry, shown schematically in Figure S4. Single-photon emission events were registered by a microchannel plate photomultiplier tube detector (R3809U, Hamamatsu, UK) and analysed by a modular TCSPC system (Ortec, UK) interfaced with a desktop computer. On-sample laser powers were controlled using a graduated neutral density filter to maintain the photon count rate below 1% of the excitation repetition rate to ensure the absence of pulse pile-up effects.

Fluorescence was collected for approximately 30 minutes from each sample and a rotating analysing polariser driven by a PC-controlled stepper motor alternately transmitted emission events polarised parallel ($\parallel$) and perpendicular ($\perp$) to the excitation polarization every 10 s, with the resulting decays $I_{\parallel}(t)$ and $I_{\perp}(t)$ stored separately in computer memory. From these two measurements, both the fluorescence and anisotropy decays could be reconstructed, enabling the study of both excited state decay rates and orientational dynamics[9]. The setup was confirmed to exhibit no polarisation bias (a G factor of unity[10]) by rotating the excitation polarization through 90° using a half-wave plate and observing that the fluorescence intensities detected for a reference sample of OG in methanol with both analyser settings ($\parallel$ and $\perp$) were equal.

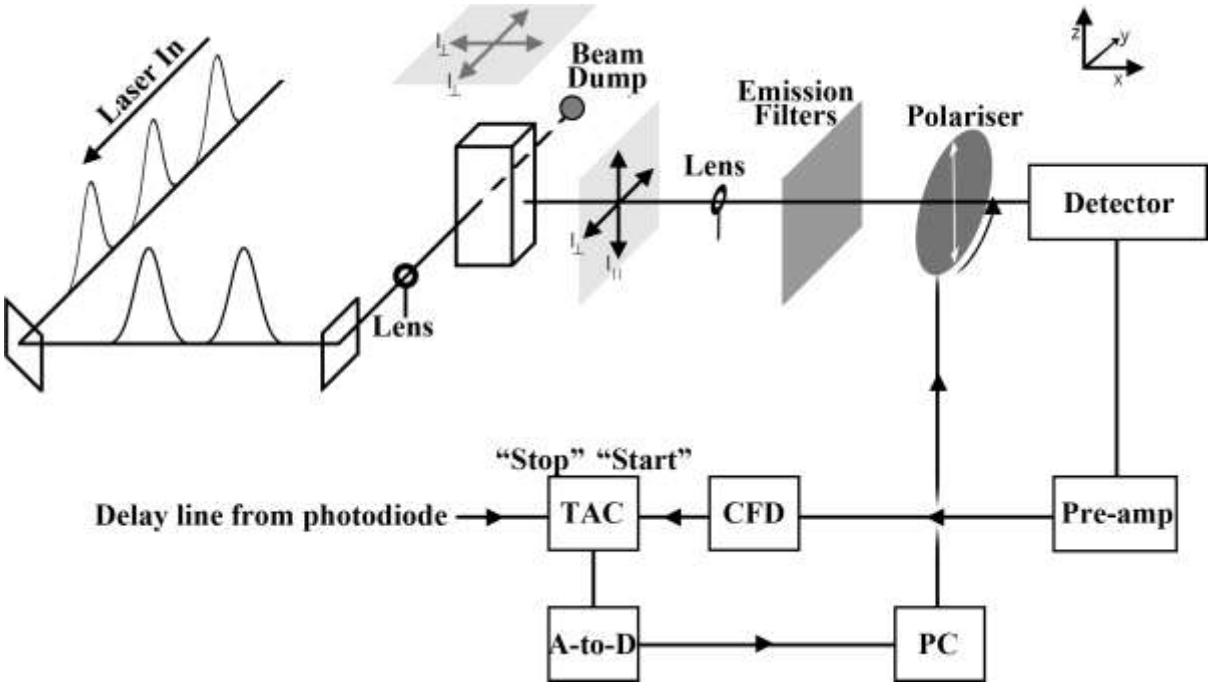

Figure S4: Schematic diagram of the TCSPC apparatus used in this work. The constant fraction discriminator (CFD) outputs a trigger current when the detector signal reaches a particular fraction of its overall height to account for amplitude jitter caused by the random signal amplification mechanism of the detector. The delay time between excitation and detection is measured in the time to amplitude converter (TAC), the output of which is digitised and stored in the PC. Datasets with the analysing polariser with the transmission axis aligned vertically $I_{\parallel}(t)$ and horizontally $I_{\perp}(t)$ are stored separately in memory, to allow the calculation of both fluorescence intensity $I(t)$ and anisotropy $R(t)$ decays.

Appendix S4: Fluorescence and anisotropy decay fitting

Fluorescence intensity decays $I(t)$ were constructed from the polarised intensity decays $I_{\parallel}(t)$ and $I_{\perp}(t)$ according to[11],

$$I(t) = I_{\parallel}(t) + 2I_{\perp}(t) \tag{S3}$$

Fluorescence lifetimes were extracted from these datasets by non-linear least squares fitting of a multi-exponential decay model,

$$I(t) = I(0)\sum_i A_i \exp(-t/\tau_i) \tag{S4}$$

where A_i represent the fraction of each species present with lifetime τ_i.

The fluorescence anisotropy was constructed from,

$$R(t) = \frac{I_{\parallel}(t) - I_{\perp}(t)}{I_{\parallel}(t) + 2I_{\perp}(t)} \tag{S5}$$

In solution, $R(t)$ for a freely diffusing cylindrically molecular probe can, in principle, be characterised by a sum of up to three exponential decay components, depending on the shape of the molecule and the molecular frame orientation of its emission transition dipole moment[12–14]. However, for symmetric rotors, provided the diffusion coefficients perpendicular and parallel to the molecular symmetry axis are of a comparable magnitude, $R(t)$ is well approximated by a single exponential decay[15,16]. For restricted rotational diffusion taking place within or as part of a larger isotropically diffusing host, two anisotropy decay times are typically observed[17] with the amplitudes and lifetimes extracted related to the half-angle of the cone in which the fluorophore is restricted, its diffusion coefficient and the overall tumbling time[12,18]. This was the case for the fluorescent protein tagged PDK1 constructs we studied previously[4]. More complicated "cone within a cone" anisotropy decays are observed for less rigidly bound fluorescent probes, such as those attached to the flexible reactive centre loop of serpins[19]. For fully flexible molecules, in which both host and probe may move relative to a common centre of mass, a trumbbell model of the biexponential fluorescence anisotropy decay is more applicable[20]. These dynamics may be expected for the

acceptor motion in the current work (see Appendix S5), with both GST and mC being of a similar size (26 kDa for GST and 28.8 kDa for mC[21,22]).

In a heterogeneous population of species i with different lifetimes τ_i and anisotropy decays $R_i(t)$, the observed fluorescence anisotropy decay is given by[19],

$$R(t,\Delta\lambda) = \sum_i W_i(t,\Delta\lambda) R_i(t) \tag{S6}$$

where $W_i(t,\Delta\lambda)$ is the time-dependent weighting factor of component i in a particular emission wavelength range $\Delta\lambda$,

$$W_i(t,\Delta\lambda) = \frac{A_i(\Delta\lambda)\exp\left(\frac{-t}{\tau_i}\right)}{\sum_j A_j(\Delta\lambda)\exp\left(\frac{-t}{\tau_j}\right)} \tag{S7}$$

$A_i(\Delta\lambda)$ represents the initial detection amplitude of species i and is dependent on the initial population size and the spectral detection efficiency of the apparatus.

Goodness-of-fit of intensity and anisotropy decay models was judged by minimisation of the χ^2_R statistic, defined as,

$$\chi^2_R = \frac{1}{n-l}\sum_{k=1}^{n}\frac{1}{\sigma_k^2}\left[I_{data}(t_k) - I_{model}(t_k)\right]^2 \tag{S8}$$

where n is the total number of data points and l is the number of free parameters in the model. σ_k is the expected standard deviation of the kth data point. As single-photon counting measurements follow Poisson statistics, the expected standard deviation of $I_{\parallel}(t)$ and $I_{\perp}(t)$ are $\sqrt{I_{\parallel}(t)}$ and $\sqrt{I_{\perp}(t)}$ respectively. Propagation of error[23] then leads to,

$$\sigma_k^2 = I_{\parallel}(t_k) + 4I_{\perp}(t_k) \tag{S9}$$

For calculation of χ^2_R in anisotropy decay fitting, propagation of uncertainty through equation S5 leads to the more complex weighting function[23],

$$\sigma_k^2 = \frac{1}{\left[I_{\parallel}(t_k) + 2I_{\perp}(t_k)\right]^4} \begin{pmatrix} \left[I_{\parallel}(t_k) + 4I_{\perp}(t_k)\right]\left[I_{\parallel}(t_k) - I_{\perp}(t_k)\right]^2 \\ -2\left[I_{\parallel}(t_k) - 2I_{\perp}(t_k)\right]\left[I_{\parallel}(t_k) - I_{\perp}(t_k)\right]\left[I_{\parallel}(t_k) + 2I_{\perp}(t_k)\right] \\ +\left[I_{\parallel}(t_k) + I_{\perp}(t_k)\right]\left[I_{\parallel}(t_k) + 2I_{\perp}(t_k)\right]^2 \end{pmatrix} \quad \text{(S10)}$$

In this work, the best-fit model was chosen as that to which the addition of further components caused no further decrease in χ_R^2 while maintaining a mean Levenberg-Marquardt standard error[24] in the fit parameters $\overline{\Delta p}$ below 50%. As the temporal response of the TCSPC system was significantly faster than the fluorescence lifetimes involved (0.08 ns instrument response function full width at half maximum), good fits could be obtained by fitting directly to the data starting at the peak of the decay (tail fitting) using Origin 8.6 (OriginLab, USA). The exception to this procedure was in the fitting of the acceptor window fluorescence decay during FRET. Here, reconvolution of the model with the instrument response function, obtained by performing a TCSPC measurement on a scattering solution, was required in order to obtain a good fit (χ_R^2 < 2) to the negative amplitude rise components. This was carried out using the Fluofit analysis package (Picoquant, Germany).

Appendix S5: Fundamental photophysics of OG-GSH and GST-mC

Measurements of the fluorescence decay of OG-GSH were made with 475 nm and 498 nm single-photon excitation and two-photon excitation at 880 nm. The results of these measurements are summarised in Table S1 and an example fit is shown in Figure S5. A mean lifetime across the excitation wavelengths of 4.26 (±0.06) ns was obtained, in agreement with previously reported values[2].

To determine the nature of the excited states in mC that are accessed by unrestricted FRET transfer, single-photon excitation of GST-mC was undertaken at wavelengths spanning the donor-acceptor overlap (475-615 nm) with fluorescence detected in the acceptor window (630-650 nm). The data was best fit to two decay components whose lifetime and relative amplitude variation with excitation wavelength are shown in Table S2. The bi-exponential decay yielded an amplitude-weighted mean GST-mC fluorescence lifetime averaged across the excitation wavelengths of 1.559 (±0.002) ns and parameter uncertainties below 1%. The average χ_R^2 for a one-component fit was 6.7 (±0.6). Addition of a third decay component did not improve χ_R^2 beyond that of the bi-exponential fit ($1.0 \le \chi_R^2 \le 1.5$) yielding a mean value of $\chi_R^2 = 1.22(\pm 0.04)$ with large corresponding mean lifetime and amplitude uncertainties of ~10^5 %. A representative decay trace with fitting parameters is shown in figure S6 and the variation in the GST-mC fluorescence decay parameters across the spectral overlap are plotted in figure S7. Between 475 nm and 565 nm, the lifetimes of both fluorescence decay components remained unchanged at 1.33(±0.01) ns and 1.92 (±0.02) ns respectively. At longer excitation wavelengths, both lifetimes were found to decrease, however the amplitude-weighted average lifetime remained constant through an increase in the relative weighting of the longer lifetime component. These observations are consistent with previous donor-acceptor overlap excitation measurements in recombinant mC[4].

Fluorescence anisotropy decays were constructed from the polarised fluorescence decays $I_{\parallel}(t)$ and $I_{\perp}(t)$ (equation S5). Immediately after excitation, the fluorescence anisotropy of OG-GSH, averaged across the single-photon excitation measurements, was 0.37(±0.01), indicating approximately collinear absorption and emission dipole moments[9]. A representative decay is shown in figure S8. With two-photon excitation, the initial anisotropy of 0.542(±0.006) was close to the theoretical maximum of 4/7 [25]. As can be seen in table S3, the single-photon fluorescence anisotropy decayed with a single rotational correlation time

with a mean value of 0.251(±0.008) ns. The rotational correlation time with two-photon excitation was slightly longer at 0.279(±0.003) ns.

Initial anisotropies were also close to 0.4 in GST-mC (figure S9). In contrast to OG-GSH, the anisotropy decays were clearly bi-exponential as set out in table S4, with overlap-weighted mean rotational correlation times of 1.1(±0.1) ns and 28(±1) ns. In a heterogeneous system, rapid population dynamics can yield composite anisotropy features that are considerably faster than the intrinsic rotational diffusion of the constituent populations[4]. However a composite anisotropy model (equations S6 and S7) in which each mC sub-population was assigned an individual rotational correlation time could not be fit to these datasets at any excitation wavelength (mean $\chi_R^2 = 4.8 \pm 0.5$). This indicates that the rotational dynamics are more complicated than pure rigid body rotational diffusion.

Both mC and GST are large macromolecules of comparable molecular weight with expected rotational correlation times of 21 ns and 23 ns respectively based on a rule of thumb[26] of 0.8 ns kDa^{-1}. Calculation of the hydrodynamic volumes of both proteins from their crystal structures[27] gives a common value of 43000 $Å^3$. The shortest rotational correlation time of a rigid ellipsoid is 0.95 that of an equi-volume spherical diffuser[13,28], allowing us to conclude that the fast decay component cannot be ascribed to a component of rigid body rotational diffusion. The relationship between fast anisotropy decay dynamics and internal macromolecular motions has been investigated by several authors and a number of theoretical models treating rotational and translational diffusion in flexible molecules have been advanced[28,29]. In GST-mC, the two proteins are linked by a 6 amino acid chain[30] with an approximate contour length of 2.3 nm[31]. A simple three component model for flexible macromolecules, the elastic trumbbell, has been the subject of a number of studies[32–37]. The flexible molecule is modelled as three units as shown in Figure S10. The two bonds of the trumbbell are regarded as the two cylindrically symmetric subunits of the segmentally flexible macromolecule. Distortion of the trumbell from a fully linear configuration is counteracted by a restoring potential of the form,

$$V(\alpha) = \frac{kT}{2\gamma^2}(\alpha - \alpha_0)^2 \qquad \text{(S11)}$$

where γ is the elastic constant for the bending motion. For a straight trumbbell ($\alpha_0 = 0°$) this becomes,

$$\frac{V(\alpha)}{kT} = Q\alpha^2 \tag{S12}$$

with,

$$Q = \frac{1}{2\gamma^2} \tag{S13}$$

In the limit where $\gamma \to 0$ the stiffness parameter $Q \to \infty$, corresponding to an infinitely rigid linear trumbbell. In practical terms, this is reached when $\gamma = 0.1$[20]. The fluorescence anisotropy decay of the of the molecule is given as,

$$R(t) = R(0)\langle P_2(\cos\theta_b)\rangle \tag{S14}$$

where the emission and absorption moments are along b. For values of Q ranging from 50 to 0.05, the practical stiffness limits of infinitely rigid and fully flexible bending motions respectively, Diaz and de la Torre have obtained, from Brownian trajectories, the expected decay functions, taking the form,

$$\langle P_2(\cos\theta_b)\rangle = a\exp\left(-\frac{t}{\tau_1}\right) + (1-a)\exp\left(-\frac{t}{\tau_2}\right) \tag{S15}$$

where τ_1 and τ_2 are the slow and fast correlation times recovered from the nonlinear least squares fit respectively. At each value of Q, the results of the simulations yield values of τ_1/τ_2, the average trumbbell angle $\langle\alpha\rangle$ and the pre-exponential factor a, as shown in Figure S11. The average (±S.D.) bi-exponential fit results from mCherry-GST fluorescence anisotropy measurements obtained for excitation wavelengths across the donor-acceptor overlap region, together with the corresponding values for the local cone angle (assuming independent local and overall rotational diffusion of mCherry), are also shown. The average experimental decay amplitudes correspond to an average bend angle of 19.5°. This is comparable to the cone angle of 14.8° calculated from the same value of a using the model

of Lipari and Szabo[12] (equations S26 and S27). The intrinsic fluorescence anisotropy of GST-mC thereby indicates restricted local motion of mC within an approximately linear structure.

λ_{ex} / nm	Emission Window	τ / ns	χ_r^2	$\overline{\Delta p}$ / %
475	Donor	4.2(±0.2)	1.6	0.19(±0.03)
475	Acceptor	4.2(±0.1)	1.4	0.17(±0.02)
498	Donor	4.2(±0.1)	2.1	0.17(±0.02)
498	Acceptor	4.2(±0.1)	1.6	0.16(±0.02)
880	Donor	4.5(±0.1)	2.1	0.15(±0.01)

Table S1: Overview of the best fit parameters to fluorescence decay data obtained from 10 μM OG-GSH solutions with varying excitation and emission conditions. Donor and acceptor window decays were measured with single-photon excitation. However, with two-photon excitation and a concentration of 10 μM OG-GSH, compared to 60 μM in the FRET mixtures, count rates in the acceptor window were too low to make a measurement feasible. All datasets were best fit to a single exponential model as addition of a further component did not improve χ_R^2 and the resulting parameter errors were, on average, 120(±20)%.

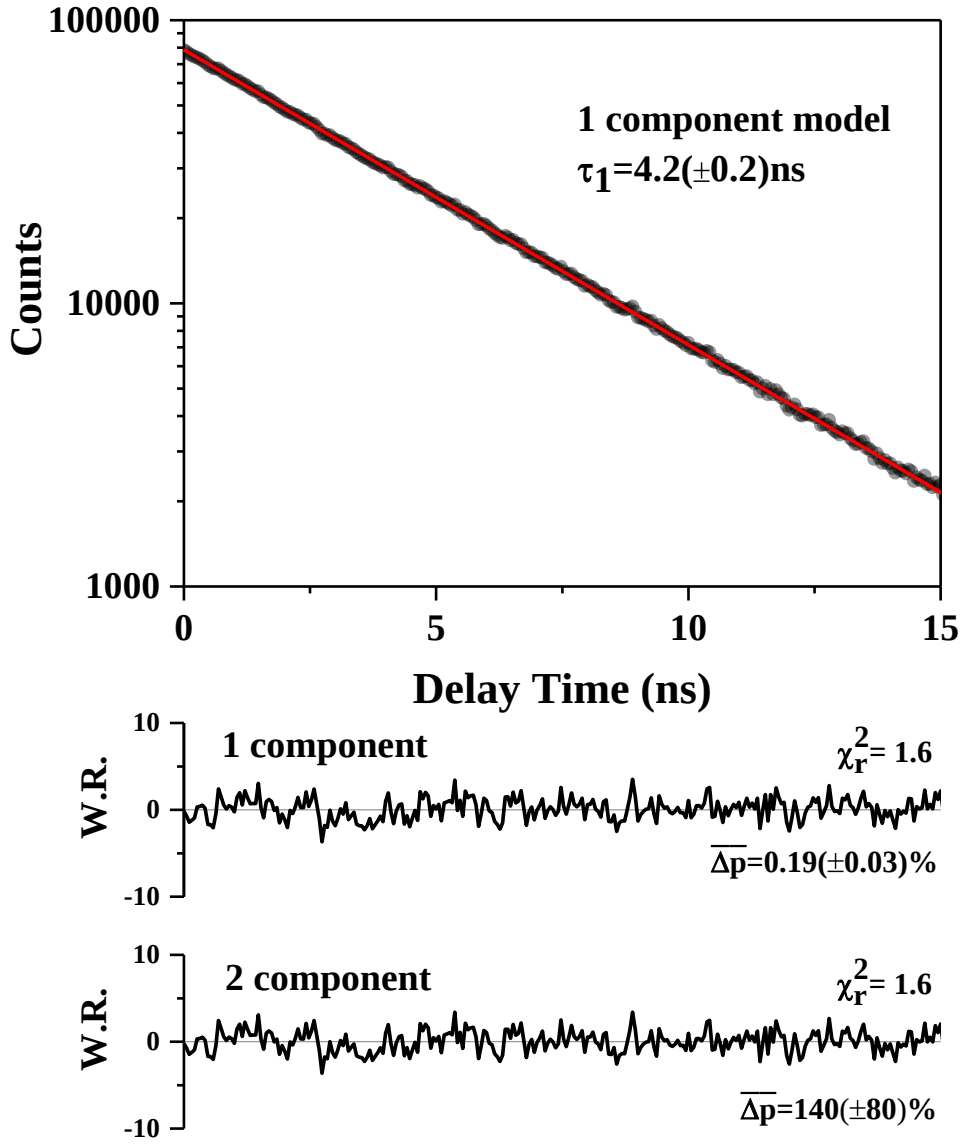

Figure S5: Representative fluorescence decay fitting from 10 μM OG-GSH with 475 nm excitation and fluorescence detection in the donor window.

λ_{ex} / nm	O(λ) / au	α_1 / %	τ_1 / ns	τ_2 / ns	<τ> / ns	χ_r^2	$\overline{\Delta p}$ / %
475	0.000	62.7(±0.1)	1.318(±0.004)	1.941(±0.005)	1.550(±0.004)	1.1	0.33(±0.04)
485	0.001	63.7(±0.1)	1.335(±0.005)	1.953(±0.006)	1.560(±0.005)	1.3	0.38(±0.04)
498	0.019	58.9(±0.2)	1.329(±0.007)	1.913(±0.008)	1.569(±0.007)	1.2	0.55(±0.06)
505	0.060	51.9(±0.2)	1.272(±0.006)	1.873(±0.005)	1.561(±0.005)	1.2	0.41(±0.06)
525	0.268	72.2(±0.1)	1.393(±0.004)	2.012(±0.007)	1.565(±0.005)	1.2	0.37(±0.07)
545	0.292	58.8(±0.1)	1.333(±0.004)	1.890(±0.005)	1.562(±0.005)	1.0	0.35(±0.04)
565	0.201	54.2(±0.2)	1.297(±0.005)	1.874(±0.005)	1.562(±0.005)	1.3	0.38(±0.05)
585	0.135	35.9(±0.2)	1.201(±0.008)	1.760(±0.003)	1.560(±0.005)	1.2	0.5(±0.1)
605	0.024	27.5(±0.2)	1.12(±0.01)	1.721(±0.003)	1.556(±0.005)	1.2	0.6(±0.2)
615	0.000	24.3(±0.2)	1.06(±0.01)	1.700(±0.003)	1.545(±0.006)	1.5	0.7(±0.3)
<O(λ)>	-	57.2(±0.2)	1.315(±0.002)	1.897(±0.003)	1.564(±0.002)	-	-

Table S2: Bi-exponential fit parameters to the (acceptor window) fluorescence decay data obtained from 4 μM GST-mC solutions at excitation wavelengths across the donor-acceptor overlap. $O(\lambda)$ is the corresponding (normalised) OG-mC FRET spectral overlap value for each excitation wavelength, allowing the overlap-weighted averages $\langle O(\lambda) \rangle$ to be calculated.

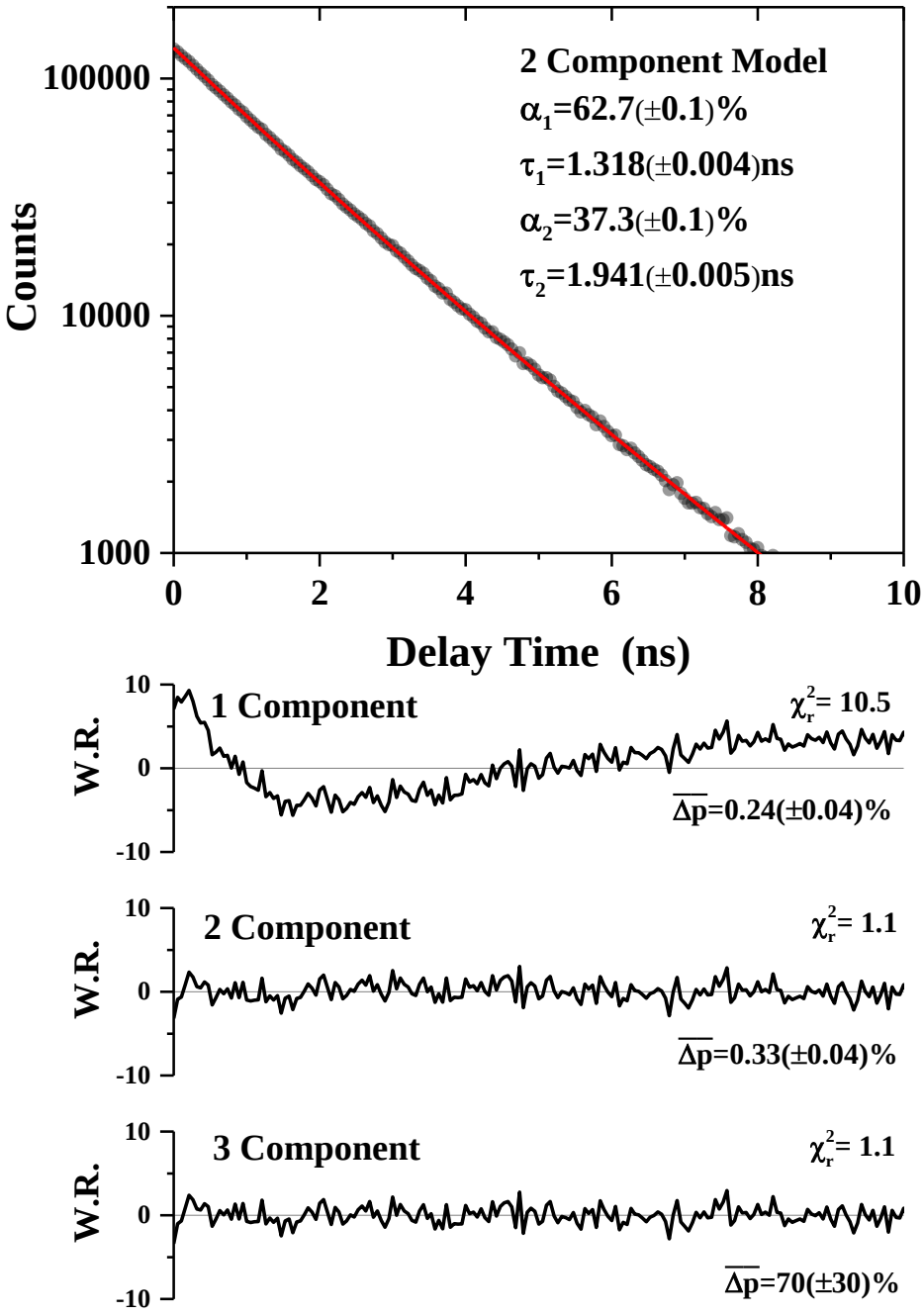

Figure S6: A representative fluorescence decay following 475nm single photon excitation of a 4 μM GST-mC solution. Single photon excitation of GST-mC spanning wavelengths between 475 nm and 615 nm was used to simulate unrestricted FRET to mC with fluorescence detection in the 630-650 nm acceptor window.

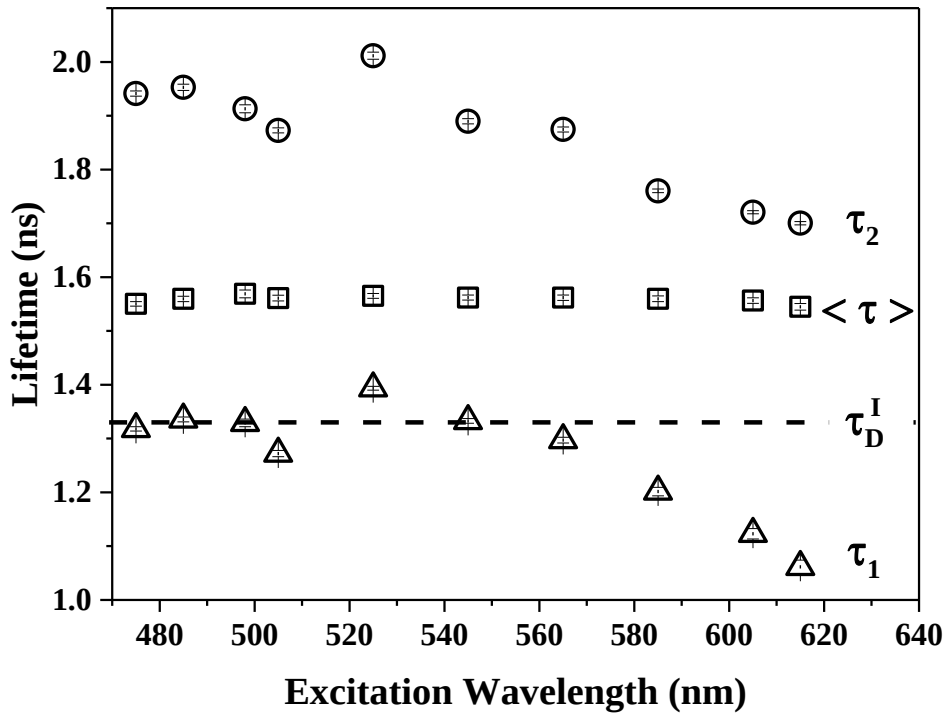

Figure S7: Summary of bi-exponential fluorescence decay parameters for GST-mC following single photon excitation at wavelengths across the donor-acceptor overlap region. The dashed line at 1.33 ns corresponds to the measured interacting donor lifetime τ_D^I. For excitation wavelengths between 475nm and 565nm, the close distribution of the values of τ_1 about τ_D^I necessitate the analysis described in Appendix S9.

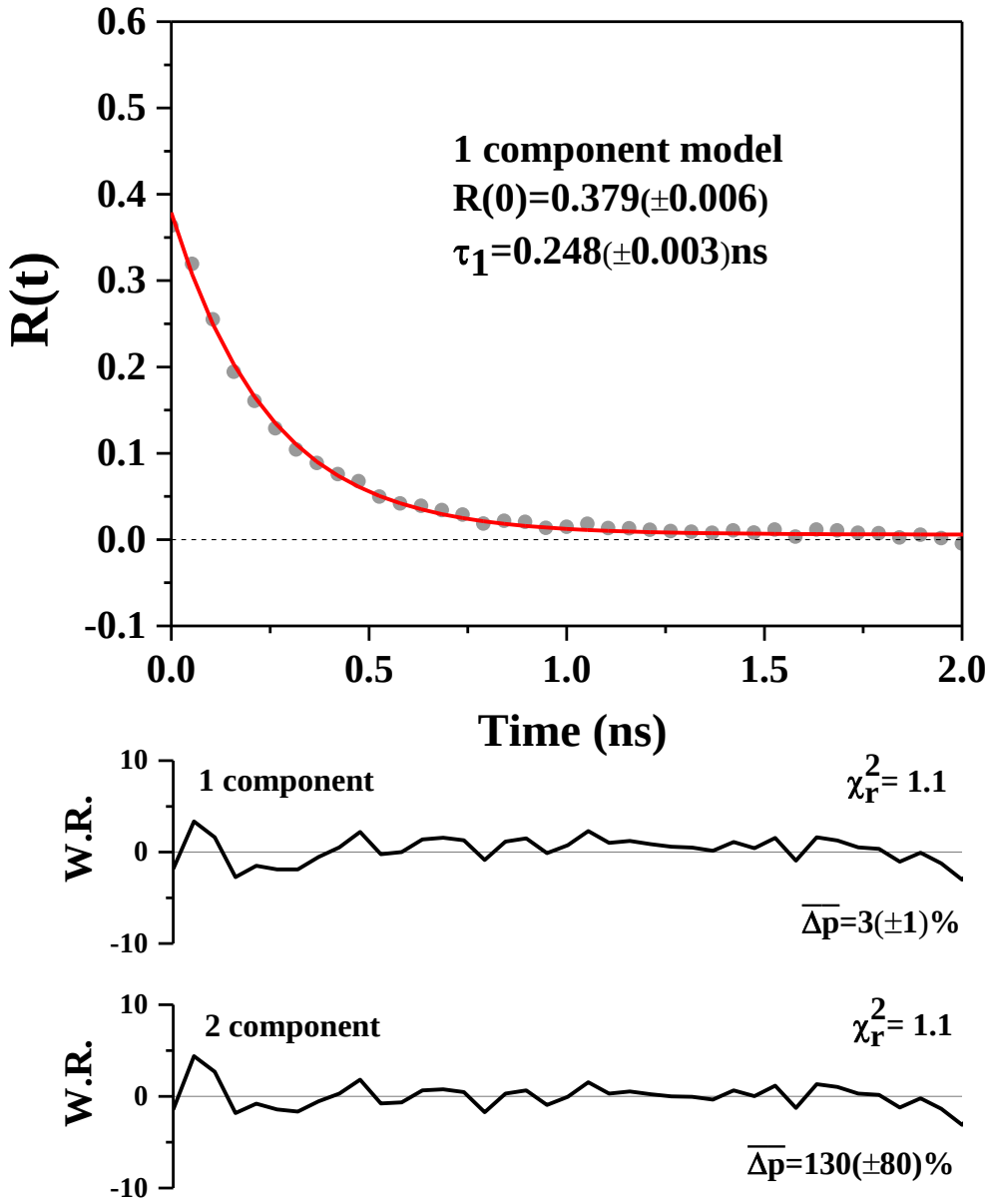

Figure S8: A representative fluorescence anisotropy decay fitting from 10 μM OG-GSH with 475 nm excitation and fluorescence detection in the donor window.

λ_{ex} / nm	Emission Window	R(0)	θ / ns	χ_r^2	$\overline{\Delta p}$ / %
475	Donor	0.379(±0.006)	0.248(±0.003)	1.1	3(±1)
475	Acceptor	0.355(±0.006)	0.234(±0.003)	1.4	8(±7)
498	Donor	0.349(±0.007)	0.259(±0.003)	1.2	1.2(±0.1)
498	Acceptor	0.390(±0.010)	0.237(±0.003)	1.3	8(±7)
880	Donor	0.542(±0.006)	0.279(±0.003)	2.0	6(±4)

Table S3: Best fit parameters to fluorescence anisotropy decay data obtained from 10 μM OG-GSH solutions with varying excitation and emission conditions.

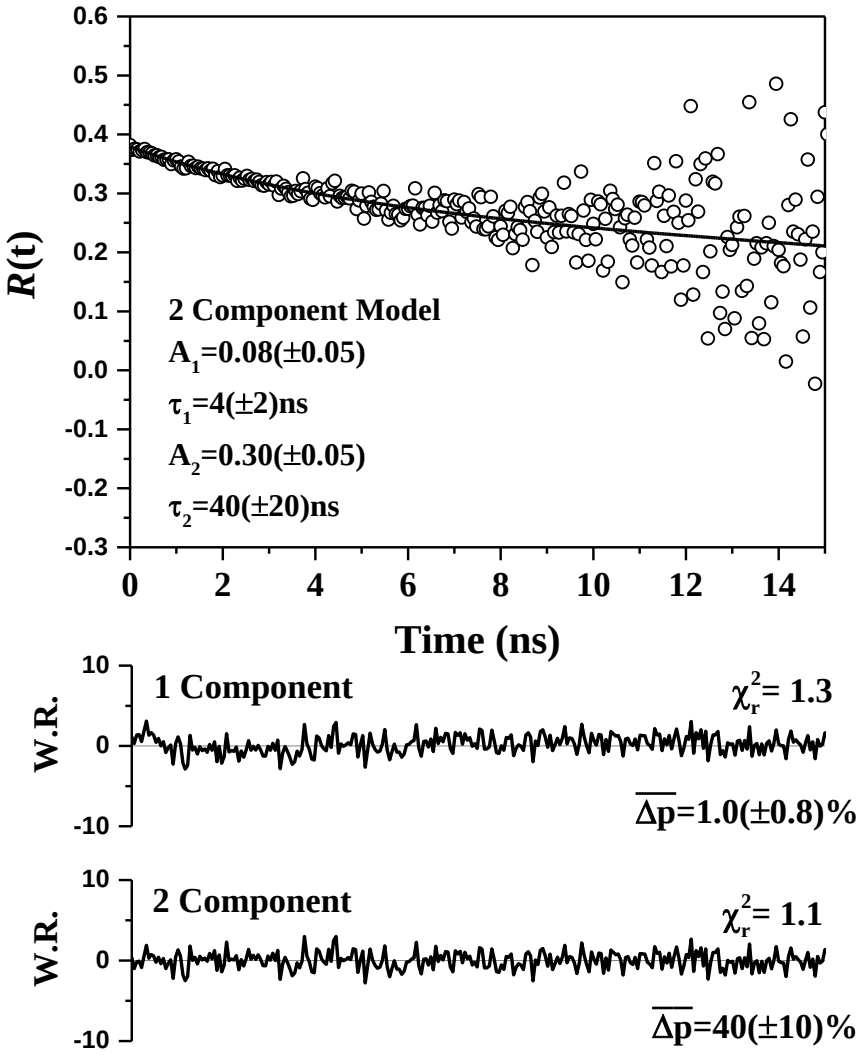

Figure S9: A representative fluorescence anisotropy decay and analysis for a donor-acceptor overlap excitation wavelength of 475 nm simulating unrestricted FRET to GST-mC (4 μM solution) with fluorescence detection between 630 nm and 650 nm (acceptor window). The fluorescence anisotropy decays are clearly bi-exponential with a short correlation time ascribed to local motion of mC and the longer rotational time corresponding to overall rotational diffusion of the two coupled proteins.

λ_{ex} / nm	O(λ) / au	R_0	a	τ_1 / ns	τ_2 / ns	χ_r^2	$\overline{\Delta p}$ / %
475	0.000	0.38(±0.07)	0.8(±0.1)	40(±20)	4(±2)	1.1	40(±10)
485	0.001	0.38(±0.01)	0.90(±0.02)	29(±3)	1.4(±0.3)	1.0	13(±5)
498	0.019	0.38(±0.01)	0.92(±0.02)	25(±3)	1.3(±0.6)	1.2	30(±10)
505	0.060	0.389(±0.004)	0.946(±0.007)	23(±1)	0.6(±0.2)	1.0	11(±6)
525	0.268	0.398(±0.009)	0.88(±0.01)	33(±3)	1.4(±0.3)	1.0	11(±4)
545	0.292	0.40(±0.01)	0.90(±0.02)	30(±3)	1.4(±0.3)	1.1	14(±5)
565	0.201	0.400(±0.003)	0.940(±0.005)	24(±1)	0.5(±0.1)	1.1	9(±5)
585	0.135	0.398(±0.006)	0.94(±0.01)	24(±1)	0.9(±0.2)	1.1	12(±6)
605	0.024	0.401(±0.004)	0.940(±0.007)	27(±1)	0.7(±0.1)	1.0	9(±5)
615	0.000	0.397(±0.003)	0.950(±0.005)	25(±1)	0.4(±0.1)	1.1	10(±6)
<O(λ)>	-	0.398(±0.003)	0.912(±0.007)	28(±1)	1.1(±0.1)	-	-

Table S4: Overview of best fit parameters to fluorescence anisotropy decay data obtained from 4 μM GST-mC solutions with excitation wavelengths across the donor-acceptor overlap in the donor emission window. By convention, *a* is the fractional amplitude of the longer rotational correlation time component, related to the orientational freedom of the fluorophore in the trumbbell configuration[20].

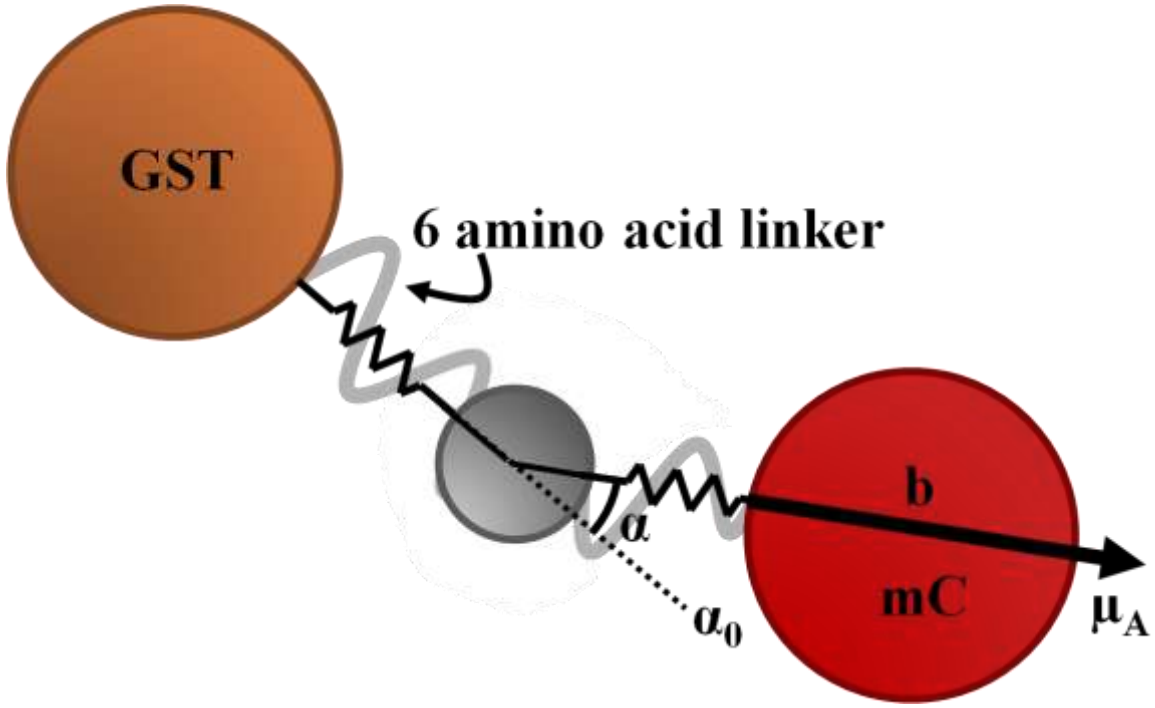

Figure S10: A schematic representation of a linear trumbbell as applied to the GST-mC construct. The equilibrium configuration has $\alpha_0 = 0°$, with a transient bending angle α. The acceptor absorption and emission transition dipole moments are taken to lie along the bond axis b. The measured fluorescence anisotropy depends on both $\alpha(t)$ and the end-to-end tumbling motion of the trumbbell. The presence of OG-GSH binding is not assumed to alter the orientational dynamics due to its considerably smaller size.

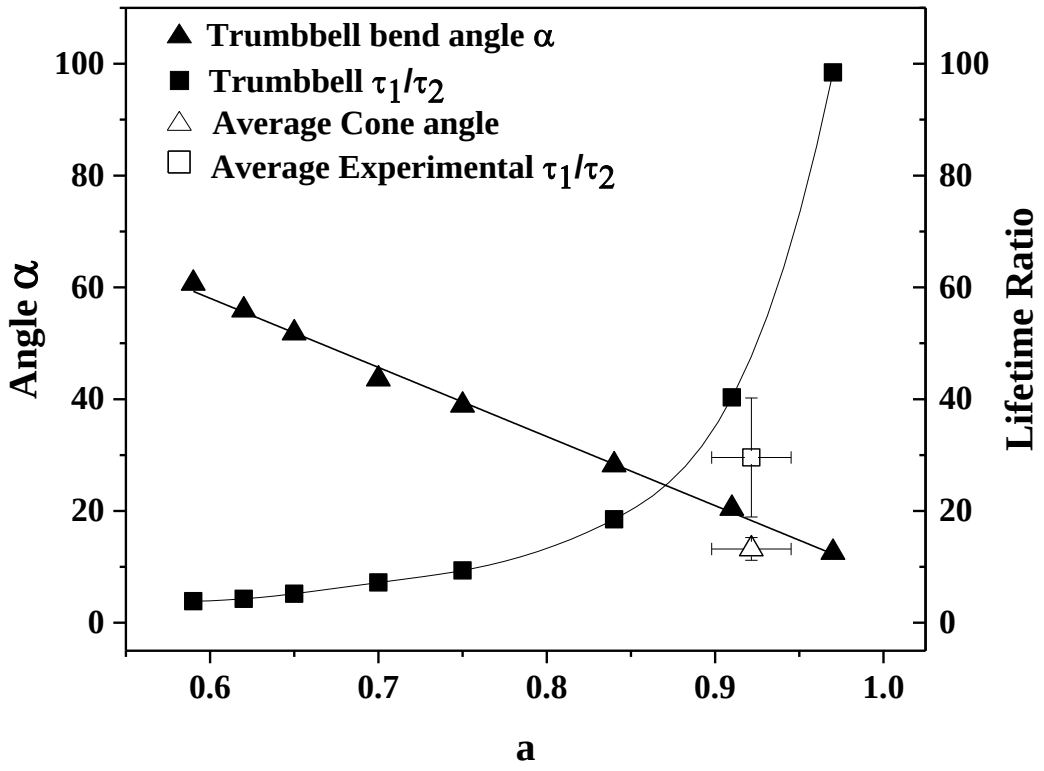

Figure S11: Results of Brownian dynamics simulations by Diaz and de la Torre[20] revealing the relationship between the bend angle of a linear trumbbell, the pre-exponential factors of its biexponential fluorescence decay and the ratio of the corresponding lifetimes (black symbols). The mean (±S.D.) lifetime ratio and amplitude for the GST-mCherry fluorescence decay measurements performed here is plotted (open square), and lies close to the theoretical results, implying a trumbbell angle of ~20°. This is close to the cone angle of ~15° calculated by using the measured amplitudes (open triangle) in the model of Lipari and Szabo[12] (equations S26 and S27).

Appendix S6: FRET dynamics with a heterogeneous acceptor population

In a FRET experiment with a single donor state and two independent acceptor states, the excited state populations of non-interacting donors and donors interacting with each acceptor state ($N_{\mathrm{D}}^{\mathrm{NI}}$, $N_{\mathrm{D1}}^{\mathrm{I}}$ and $N_{\mathrm{D2}}^{\mathrm{I}}$ respectively) and interacting and non-interacting acceptors in either of the two possible excited states ($N_{\mathrm{A1}}^{\mathrm{I}}$, $N_{\mathrm{A1}}^{\mathrm{NI}}$, $N_{\mathrm{A2}}^{\mathrm{I}}$ and $N_{\mathrm{A2}}^{\mathrm{NI}}$) would evolve, following short-pulsed excitation, according to the following set of differential equations,

$$\frac{dN_{\mathrm{D1}}^{\mathrm{I}}(t)}{dt} = -\left[k_{\mathrm{F}}^{\mathrm{D}} + k_{\mathrm{FRET1}}\right]N_{\mathrm{D1}}^{\mathrm{I}}(t) \tag{S16}$$

$$\frac{dN_{\mathrm{D2}}^{\mathrm{I}}(t)}{dt} = -\left[k_{\mathrm{F}}^{\mathrm{D}} + k_{\mathrm{FRET2}}\right]N_{\mathrm{D2}}^{\mathrm{I}}(t) \tag{S17}$$

$$\frac{dN_{\mathrm{A1}}^{\mathrm{I}}(t)}{dt} = k_{\mathrm{FRET1}}N_{\mathrm{D1}}^{\mathrm{I}}(t) - k_{\mathrm{F}}^{\mathrm{A1}}N_{\mathrm{A1}}^{\mathrm{I}}(t) \tag{S18}$$

$$\frac{dN_{\mathrm{A2}}^{\mathrm{I}}(t)}{dt} = k_{\mathrm{FRET2}}N_{\mathrm{D2}}^{\mathrm{I}}(t) - k_{\mathrm{F}}^{\mathrm{A2}}N_{\mathrm{A2}}^{\mathrm{I}}(t) \tag{S19}$$

$$\frac{dN_{\mathrm{D}}^{\mathrm{NI}}(t)}{dt} = -k_{\mathrm{F}}^{\mathrm{D}}N_{\mathrm{D}}^{\mathrm{NI}}(t) \tag{S20}$$

$$\frac{dN_{\mathrm{A1}}^{\mathrm{NI}}(t)}{dt} = -k_{\mathrm{F}}^{\mathrm{A1}}N_{\mathrm{A1}}^{\mathrm{NI}}(t) \tag{S21}$$

$$\frac{dN_{\mathrm{A2}}^{\mathrm{NI}}(t)}{dt} = -k_{\mathrm{F}}^{\mathrm{A2}}N_{\mathrm{A2}}^{\mathrm{NI}}(t) \tag{S22}$$

Here $k_{\mathrm{F}}^{\mathrm{D}}$ is the fluorescence decay rate of the non-interacting donor and $k_{\mathrm{F}}^{\mathrm{A1}}$ and $k_{\mathrm{F}}^{\mathrm{A2}}$ are the fluorescence decay rates of the two excited states of the acceptor. The rates of FRET to the two acceptor populations are k_{FRET1} and k_{FRET2}. Following our previous treatment of FRET in a multi-component system[4], equations S16-S22 are solved using the integrating factor approach and we introduce additional population decay terms to account for direct acceptor excitation (final two terms in equation S23). Time-resolved fluorescence intensities are then

calculated by multiplying each population by its radiative rate, assuming equal radiative rates for the two mC species. As a result, the wavelength dependent fluorescence intensity is given by,

$$\begin{aligned} I(t,\Delta\lambda) \propto\ & F_1^{\mathrm{I}} \exp\left(-\left(k_{\mathrm{F}}^{\mathrm{D}} + k_{\mathrm{FRET1}}\right)t\right) + F_2^{\mathrm{I}} \exp\left(-\left(k_{\mathrm{F}}^{\mathrm{D}} + k_{\mathrm{FRET2}}\right)t\right) \\ & + B(\Delta\lambda) F_1^{\mathrm{I}} X_1 \left[\exp\left(-k_{\mathrm{F}}^{\mathrm{A1}} t\right) - \exp\left(-\left(k_{\mathrm{F}}^{\mathrm{D}} + k_{\mathrm{FRET1}}\right)t\right)\right] \\ & + B(\Delta\lambda) F_2^{\mathrm{I}} X_2 \left[\exp\left(-k_{\mathrm{F}}^{\mathrm{A2}} t\right) - \exp\left(-\left(k_{\mathrm{F}}^{\mathrm{D}} + k_{\mathrm{FRET2}}\right)t\right)\right] \\ & + \left(1 - F_1^{\mathrm{I}} - F_2^{\mathrm{I}}\right) \exp\left(-k_{\mathrm{F}}^{\mathrm{D}} t\right) \\ & + B(\Delta\lambda)\delta \frac{N_{\mathrm{A1}}^{\mathrm{GS}}}{N_{\mathrm{D}}^{\mathrm{GS}}} \exp\left(-k_{\mathrm{F}}^{\mathrm{A1}} t\right) \\ & + B(\Delta\lambda)\delta \frac{N_{\mathrm{A2}}^{\mathrm{GS}}}{N_{\mathrm{D}}^{\mathrm{GS}}} \exp\left(-k_{\mathrm{F}}^{\mathrm{A2}} t\right) \end{aligned} \tag{S23}$$

where F_1^{I} and F_2^{I} are the fractions of total donors that are interacting via FRET with acceptor states 1 and 2 and $N_{\mathrm{D}}^{\mathrm{GS}}$, $N_{\mathrm{A1}}^{\mathrm{GS}}$ and $N_{\mathrm{A2}}^{\mathrm{GS}}$ are the ground state donor and acceptor populations. The transfer amplitudes to the two acceptor states X_1 and X_2 are related to the fluorescence decay and FRET rates by,

$$X_1 = \frac{k_{\mathrm{FRET1}}}{k_{\mathrm{F}}^{\mathrm{D}} + k_{\mathrm{FRET1}} - k_{\mathrm{F}}^{\mathrm{A1}}} \tag{S24}$$

$$X_2 = \frac{k_{\mathrm{FRET2}}}{k_{\mathrm{F}}^{\mathrm{D}} + k_{\mathrm{FRET2}} - k_{\mathrm{F}}^{\mathrm{A2}}} \tag{S25}$$

The parameter δ is the ratio of absorption efficiencies of the acceptor and donor at the chosen excitation wavelength. Low values of δ (<< 1) are desirable for FRET studies to ensure that direct acceptor excitation is minimised.

Appendix S7: Composite donor window model for OG-GSH/GST-mCherry anisotropy

A fluorescent probe undergoing restricted rotational diffusion as part of a larger complex tumbling with a rotational correlation time τ_{slow} will exhibit a biexponential fluorescence anisotropy decay[18,38],

$$R(t) = R(0)\left[A\exp\left(-t/\tau_{\text{fast}}\right) + (1-A)\exp\left(-t/\tau_{\text{slow}}\right)\right] \tag{S26}$$

The angle through which the probe diffuses is related to the decay amplitude A by,

$$\cos\psi_C = \frac{-1 \pm \sqrt{1+8\sqrt{(1-A)}}}{2} \tag{S27}$$

The restricted rotational diffusion will take place with a correlation time of,

$$\tau_{\text{cone}} = \frac{1}{\left(\frac{1}{\tau_{\text{fast}}}\right) - \left(\frac{1}{\tau_{\text{slow}}}\right)} \tag{S28}$$

The diffusion coefficient can then be calculated from,

$$D = \frac{\left(1/\tau_{\text{fast}}\right) - \left(1/\tau_{\text{slow}}\right)}{A}\left[\begin{array}{l}\left(\frac{1-\cos\psi_C}{24}\right)\left(6+8\cos\psi_C - \cos^2\psi_C - 12\cos^3\psi_C - 7\cos^4\psi_C\right) \\ \quad - \frac{\cos^2\psi_C\left(1+\cos\psi_C\right)^2}{2\left(1-\cos\psi_C\right)}\left\{\ln\left(\frac{1+\cos\psi_C}{2}\right) + \left(\frac{1-\cos\psi_C}{2}\right)\right\}\end{array}\right] \tag{S29}$$

For an unconfined probe with $A = 1$ and $\psi_C = 180°$, this reduces to the isotropic rotational diffusion relationship of,

$$D = \frac{1}{6\tau_{\text{cone}}} \tag{S30}$$

In the donor window, the OG-GSH bound to GST-mCherry can be expected to exhibit restricted rotational diffusion as in equation S26, while unbound donor molecules will undergo isotropic rotational diffusion with the correlation time τ_{free} extracted from the isolated OG-GSH measurements. If a fraction $1-\eta_{\text{free}}$ of the non-interacting donors are,

nevertheless, bound to GST-mCherry, the associated anisotropy (equations S6 and S7) will decay according to,

$$R(t) = \frac{R(0)}{(1-F_{\mathrm{I}})\exp\left(-t/\tau_{\mathrm{D}}^{\mathrm{NI}}\right) + F_{\mathrm{I}}\exp\left(-t/\tau_{\mathrm{D}}^{\mathrm{I}}\right)} \left[\begin{array}{l} \eta_{\mathrm{free}}(1-F_{\mathrm{I}})\exp\left(-t/\tau_{\mathrm{D}}^{\mathrm{NI}}\right)\exp\left(-t/\tau_{\mathrm{free}}\right) \\ + F_{\mathrm{I}}\exp\left(-t/\tau_{\mathrm{D}}^{\mathrm{I}}\right)\left[A\exp\left(-t/\tau_{\mathrm{fast}}\right) + (1-A)\exp\left(-t/\tau_{\mathrm{slow}}\right)\right] \\ + (1-\eta_{\mathrm{free}})(1-F_{\mathrm{I}})\exp\left(-t/\tau_{\mathrm{D}}^{\mathrm{NI}}\right)\left[A\exp\left(-t/\tau_{\mathrm{fast}}\right) + (1-A)\exp\left(-t/\tau_{\mathrm{slow}}\right)\right] \end{array}\right] \quad \text{(S31)}$$

where $F_{\mathrm{I}} = F_1^{\mathrm{I}} + F_2^{\mathrm{I}}$ and only one interacting lifetime is present in the donor window fluorescence decay, as in this work. This model could be fit by varying only η_{free}, A and τ_{fast}, holding the values of the other parameters constant from their measurement in the isolated donor or acceptor. In order to reduce degrees of freedom, the assumption was made that the global tumbling time of the OG-GSH-GST-mCherry complex was equal to that of isolated GST-mCherry. As the binding of OG-GSH to GST-mCherry causes an increase in mass of only 3%, this approximation appears valid.

The weighting factors for the interacting and non-interacting OG-GSH populations, $W_{\mathrm{I}}(t)$ and $W_{\mathrm{NI}}(t)$, are given by the exponential fluorescence intensity decays of interacting and non-interacting OG-GSH, with decay constants of $\tau_{\mathrm{D}}^{\mathrm{I}}$ and $\tau_{\mathrm{D}}^{\mathrm{NI}}$ respectively. The difference in these values will cause the contribution of fluorescence from OG-GSH that is undergoing FRET relative to the total fluorescence intensity to vary with time, given by,

$$\frac{F_{\mathrm{I}}W_{\mathrm{I}}(t)}{F_{\mathrm{I}}W_{\mathrm{I}}(t) + (1-F_{\mathrm{I}})W_{\mathrm{NI}}(t)} = \frac{F_{\mathrm{I}}\exp\left(-t/\tau_{\mathrm{D}}^{\mathrm{I}}\right)}{F_{\mathrm{I}}\exp\left(-t/\tau_{\mathrm{D}}^{\mathrm{I}}\right) + (1-F_{\mathrm{I}})\exp\left(-t/\tau_{\mathrm{D}}^{\mathrm{NI}}\right)} \quad \text{(S32)}$$

For $\tau_{\mathrm{D}}^{\mathrm{I}} = 1.33$ ns, $\tau_{\mathrm{D}}^{\mathrm{NI}} =$ 4.213 ns and $F_I =$ 0.136, the contribution from OG-GSH undergoing FRET decreases to 5.3% by 2 ns.

Appendix S8: Resolving discrepancies in GSH-GST K_D measurements

The OG-GSH-GST-mC system has previously been used to measure the dissociation constant K_D of GSH and GST inside live cells[30]. However, at 37.2(±0.2) μM, the value obtained was almost double that of the literature value of 20 μM[39]. While the intracellular microenvironment, including the presence of endogenous GSH, may have contributed to this discrepancy, we sought to understand the impact on these measurements of the 28(±3)% FRET-inactive GST-mC population revealed here by the donor window anisotropy decay. Based on the analysis of Chen et al.[30], the dissociation constant inferred from measurements in which all GST-mC was assumed to undergo FRET (K_D^{FRET}) can be adjusted for the presence of a FRET-inactive population of GST-mC of concentration $[A']$ by,

$$K_D^{Adjusted} = K_D^{FRET}\left(1 - \frac{[A']}{[A^*]}\frac{F_I}{1-F_I}\right) \quad \text{(S33)}$$

where F_I is the interacting donor fraction provided by the FRET measurement and $[A^*]$ is the total concentration of both FRET active and inactive GST-mC. Our measurements revealed the FRET-inactive fraction of GST-mC to be $[A']/[A^*] = 0.28(\pm 0.03)$. For the measured intracellular F_I values of between 60 and 70%[30], equation S33 gives $K_D^{Adjusted}$ between 13(±3) μM and 22(±2) μM, in better agreement with published (in solution) data[39]. This highlights the useful role that donor window anisotropy measurements can play in identifying associating but non-FRET active species in biochemical equilibria.

Appendix S9: Potential discontinuities and sign changes in the X_1 FRET amplitude

The acceptor window fluorescence intensity decay dynamics of OG-GSH/GST-mCherry mixtures are governed by equation S23, where it can be seen that the amplitudes of the sensitised acceptor components are dependent on the respective transfer amplitudes to the two excited states, X_1 and X_2. By replacing the fluorescence decay rates in equations S24 and S25 with the lifetimes output by the TCSPC experiments,

$$X_i = \frac{\left(1/\tau_{\mathrm{D}}^{\mathrm{I}}\right) - \left(1/\tau_{\mathrm{D}}^{\mathrm{NI}}\right)}{\left(1/\tau_{\mathrm{D}}^{\mathrm{I}}\right) - \left(1/\tau_{\mathrm{A}}^{i}\right)} \tag{S34}$$

it can be seen these parameters are highly sensitive to the difference between the fluorescence lifetimes of the acceptor state and the interacting donor population. If the interacting lifetime of a given donor sub-population is shorter than the fluorescence lifetime of the corresponding acceptor, X is positive. This causes the lifetime of the negative amplitude component (rise lifetime) to be the lifetime of the interacting donor and the lifetime of the positive amplitude component (decay lifetime) will be the fluorescence lifetime of the corresponding acceptor population. Conversely, X will become negative if the fluorescence lifetime of the acceptor state is shorter than the lifetime of the donor when undergoing FRET, causing a rise component (negative amplitude) with the lifetime of the acceptor state and a decay component (positive amplitude) with the interacting donor lifetime. Comparison of the directly excited GST-mCherry fluorescence lifetimes summarised in Table S4 and the donor window fluorescence lifetimes observed in the OG-GSH GST-mCherry mixtures (figure S7) revealed that the acceptor in this FRET pair can possess fluorescence lifetimes τ_{A}^{i} close to and either side of the interacting donor fluorescence lifetime $\tau_{\mathrm{D}}^{\mathrm{I}}$. Transfer amplitudes in this construct could therefore be extremely large in both the positive and negative direction across the spectral overlap.

To understand how infinities and changes in sign may impact the shape of the time-resolved acceptor fluorescence signal, model curves were plotted based on Equation 3 with the lifetime of a single acceptor state varied either side of $\tau_{\mathrm{D}}^{\mathrm{I}}$, as shown in Figure S12. Despite $X \to \infty$ at $\tau_{\mathrm{D}}^{\mathrm{I}} = \tau_{\mathrm{A}}$, there were no discontinuities in the shape of the decays. This reflects the total fluorescence intensity of the acceptor, given by[40],

$$\int_0^\infty I_{\mathrm{A}}(t)\,dt \propto \int_0^\infty X\left\{\exp\left(-t/\tau_{\mathrm{A}}\right)-\exp\left(-t/\tau_{\mathrm{D}}^{\mathrm{I}}\right)\right\}dt = X\left(\tau_{\mathrm{A}}-\tau_{\mathrm{D}}^{\mathrm{I}}\right)=\tau_{\mathrm{A}}\left(1-\frac{\tau_{\mathrm{D}}^{\mathrm{I}}}{\tau_{\mathrm{D}}^{\mathrm{NI}}}\right) \tag{S35}$$

Thus, $\tau_{\mathrm{A}}-\tau_{\mathrm{D}}^{\mathrm{I}}\to 0$ as $X\to\infty$ and the product is a linear relationship between the fluorescence intensity of the acceptor and its lifetime.

To reduce the complexity of the theoretical models underpinning the analysis of the OG-GSH-GST-mCherry FRET pair, it is desirable to make the assumption that the two acceptor states in mCherry each possess just a single lifetime, despite their varied values across different excitation wavelengths. We have previously approximated these values as averages of each lifetime in the biexponential decay of mCherry at each optical excitation wavelength weighted by the spectral overlap at that point[4]. To confirm that this is a valid approach in the presence of potentially large and negative X values, we compared the shapes of time-resolved acceptor fluorescence models based on either the approximation of two acceptor lifetimes weighted by the spectral overlap or the 16 unique acceptor species summarised in table S2, with the relative abundance of each species dictated by the normalised overlap value at that wavelength. Written mathematically, the following functions were compared;

$$\overline{I_A(t)} = X_1\left[\exp\left(-t/\overline{\tau_A^{i=1}}\right)-\exp\left(-t/\tau_D^I\right)\right]+X_2\left[\exp\left(-t/\overline{\tau_A^{i=2}}\right)-\exp\left(-t/\tau_D^I\right)\right] \tag{S36}$$

$$I_A(t) = \sum_\lambda O_\lambda \begin{Bmatrix} X_1^{\lambda}\left[\exp\left(-t/\tau_A^{\lambda,i=1}\right)-\exp\left(-t/\tau_D^I\right)\right] \\ +X_2^{\lambda}\left[\exp\left(-t/\tau_A^{\lambda,i=2}\right)-\exp\left(-t/\tau_D^I\right)\right] \end{Bmatrix} \tag{S37}$$

where,

$$\overline{\tau_A^i} = \sum_\lambda O_\lambda \tau_A^{\lambda,i} \tag{S38}$$

$$X_i^{\lambda} = \frac{\left(1/\tau_D^I\right)-\left(1/\tau_D^{NI}\right)}{\left(1/\tau_D^I\right)-\left(1/\tau_A^{\lambda,i}\right)} \tag{S39}$$

Equations S36 and S37 are plotted in Figure S13A, where it can be seen that the two models appear indistinguishable. Using MATLAB, Poisson noise was applied to the functions with a magnitude consistent with the signal levels obtained in the acceptor window FRET

measurements in this work (peak ~5000) as shown in figure S13B. The difference between the two functions was then calculated (figure S13C). Weighting these differences by those expected for two Poisson processes (if $\sigma(A)=\sqrt{A}$ and $\sigma(B)=\sqrt{B}$, $\sigma(A-B)=\sqrt{A+B}$) showed no systematic deviations about the x axis, meaning any slight differences between equations S36 and S37 would be unresolvable with the signal levels acquired here. Assuming distinct, overlap-weighted average lifetimes of the two acceptor states was therefore valid.

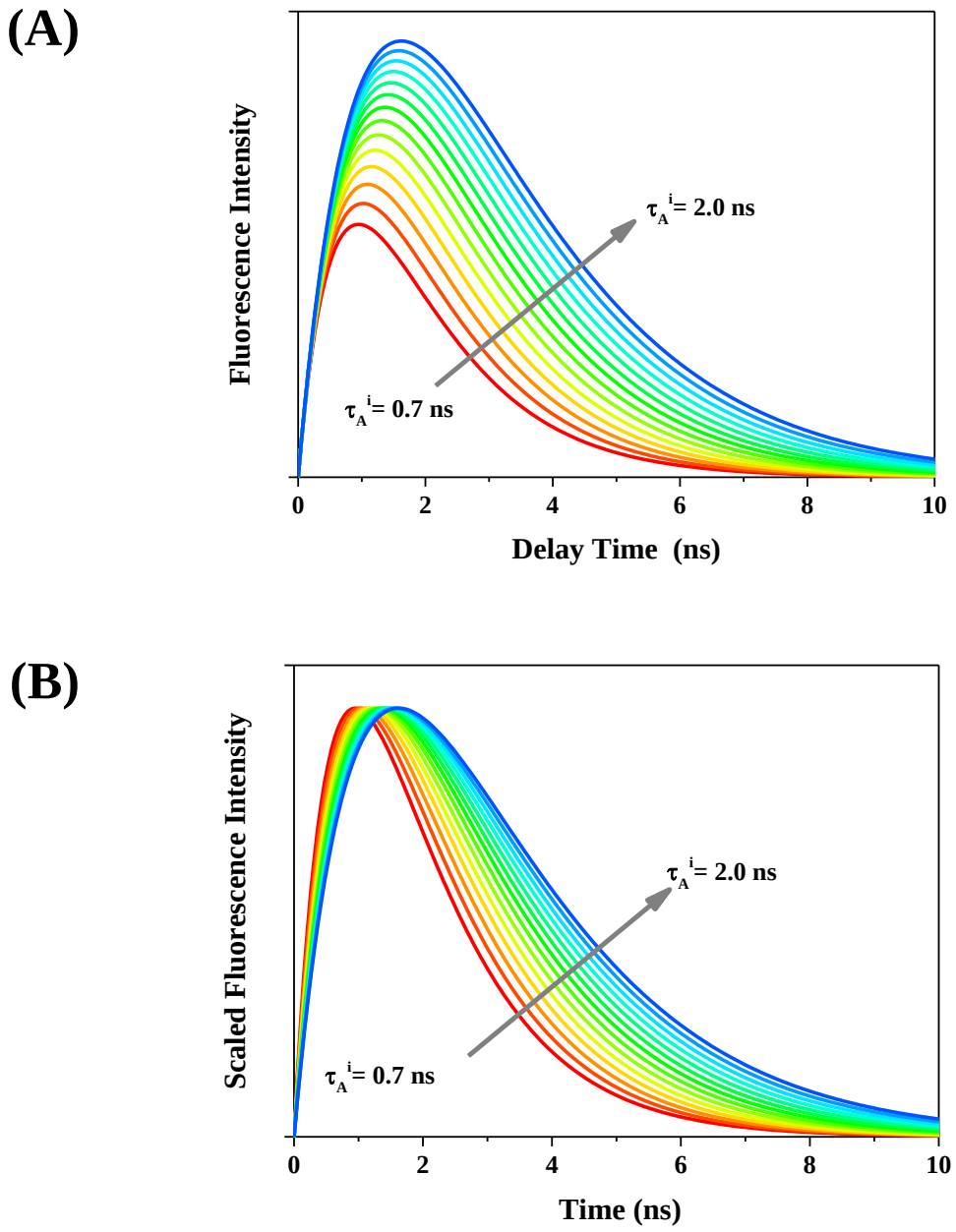

Figure S12: Time resolved acceptor fluorescence curves for GST-mCherry lifetimes either side of τ_D^I, based on equations 3 and S34 with $B \to \infty$. Despite $X \to \infty$ at $\tau_D^I = \tau_A^I$, there were no discontinuities in the shape of the fluorescence decay.

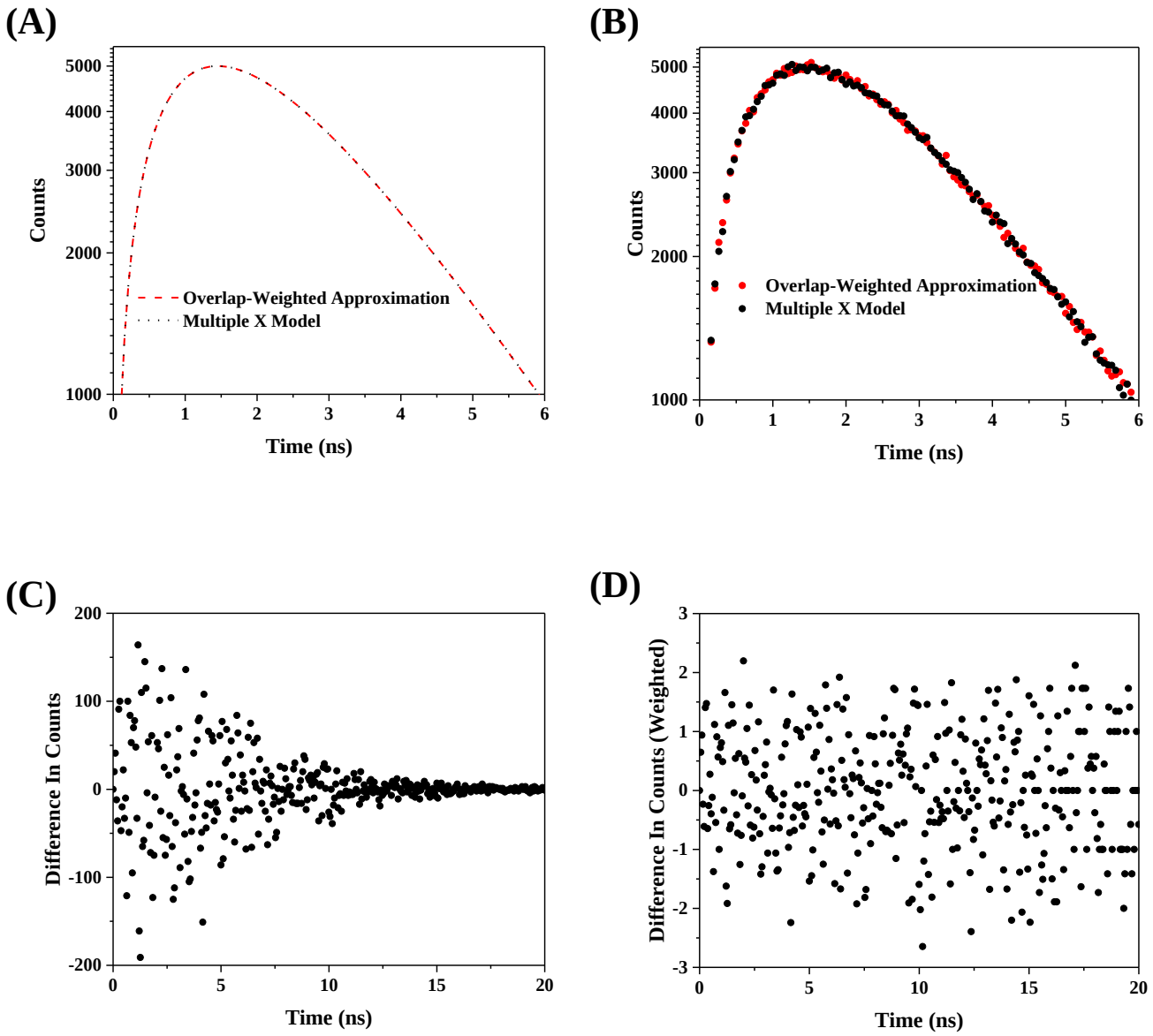

Figure S13: Comparison of the acceptor fluorescence decay with the approximation of two acceptor lifetimes determined from overlap-weighted mean values and that expected from the 16 distinct acceptor lifetimes summarised in table S2. At the signal to noise levels obtained in this work, the two functions were indistinguishable.

Appendix S10: Quantification of total non-interacting donor bleed through

The parameter B arising from the solution of equations S16 to S22 describes the specificity of a given spectral window for donor or acceptor fluorescence, based on the radiative rates of the fluorophores involved and the transmission of their fluorescence through the emission filters used. In the acceptor window, this parameter is clearly related to the contribution that donor bleed through makes to the total fluorescence detected. To quantify this, the integral relationship between the total intensity emitted by a fluorophore and the functional form of its fluorescence decay can be used[40],

$$\langle I \rangle = \int_0^\infty I(t)dt = I(0)\int_0^\infty \exp(-t/\tau)dt = I(0)\tau \tag{S40}$$

From Equation 3, the total fluorescence intensities of donor bleed through interacting with GST-mCherry through FRET ($\langle I_{\mathrm{D}}^{\mathrm{I}} \rangle$), non-interacting donor bleed through ($\langle I_{\mathrm{D}}^{\mathrm{NI}} \rangle$) and sensitised acceptor fluorescence ($\langle I_{\mathrm{A}}^{\mathrm{I}} \rangle$) can therefore be written as,

$$\langle I_{\mathrm{D}}^{\mathrm{I}} \rangle = \int_0^\infty I_{\mathrm{D}}^{\mathrm{I}}(t)dt = (F_1^{\mathrm{I}} + F_2^{\mathrm{I}})\tau_{\mathrm{D}}^{\mathrm{I}} \tag{S41}$$

$$\langle I_{\mathrm{D}}^{\mathrm{NI}} \rangle = \int_0^\infty I_{\mathrm{D}}^{\mathrm{NI}}(t)dt = (1 - F_1^{\mathrm{I}} - F_2^{\mathrm{I}})\tau_{\mathrm{D}}^{\mathrm{NI}} \tag{S42}$$

$$\langle I_{\mathrm{A}}^{\mathrm{I}} \rangle = \int_0^\infty I_{\mathrm{A}}^{\mathrm{I}}(t)dt = B[F_1^{\mathrm{I}} X_1(\tau_{\mathrm{A}}^{i=1} - \tau_{\mathrm{D}}^{\mathrm{I}}) + F_2^{\mathrm{I}} X_2(\tau_{\mathrm{A}}^{i=2} - \tau_{\mathrm{D}}^{\mathrm{I}})] \tag{S43}$$

The proportion of the total fluorescence signal detected in the acceptor window arising from non-interacting donor bleed through is then given by,

$$\frac{\langle I_{\mathrm{D}}^{\mathrm{NI}} \rangle}{\langle I_{\mathrm{D}}^{\mathrm{I}} \rangle + \langle I_{\mathrm{D}}^{\mathrm{NI}} \rangle + \langle I_{\mathrm{A}}^{\mathrm{I}} \rangle} = \frac{(1 - F_1^{\mathrm{I}} - F_2^{\mathrm{I}})\tau_{\mathrm{D}}^{\mathrm{NI}}}{(F_1^{\mathrm{I}} + F_2^{\mathrm{I}})\tau_{\mathrm{FRET}} + (1 - F_1^{\mathrm{I}} - F_2^{\mathrm{I}})\tau_{\mathrm{D}}^{\mathrm{NI}} + B[F_1^{\mathrm{I}} X_1(\tau_{\mathrm{A}}^{i=1} - \tau_{\mathrm{D}}^{\mathrm{I}}) + F_2^{\mathrm{I}} X_2(\tau_{\mathrm{A}}^{i=2} - \tau_{\mathrm{D}}^{\mathrm{I}})]} \tag{S44}$$

From the values of these parameters obtained during the characterisation of isolated GST-mCherry and the fluorescence intensity decay of the FRET mixture in the donor window,

assuming equal populations of the two acceptor states, this ratio is calculated as 69.1%. For FRET only to the short lifetime state or long lifetime state in GST-mCherry, this value would change to 72.7% and 65.8% respectively. Regardless of the proportion of FRET occurring to the two available states in the heterogenous GST-mCherry population, these calculations demonstrate the significant influence of non-interacting donor bleed through in the acceptor window measurements made in this work.

Appendix S11: Relationship between acceptor window fits and FRET dynamics

In FRET to mCherry by OG, there is increased bleed through of non-interacting donor fluorescence into the acceptor window compared to the use of EGFP, with $B_{\mathrm{OG}}(\Delta\lambda_{\mathrm{D}}) = 9.7$ and $B_{\mathrm{EGFP}}(\Delta\lambda_{\mathrm{D}}) = 19.95$. The consequence of a rapidly depolarising, non-interacting donor bleed through coupled with the increased complexity of the intrinsic FRET dynamics with a mobile donor[41–43] is that, on its own, the acceptor window anisotropy decay could not provide an unequivocal indicator of FRET restriction. In this light, it was necessary to examine the structure of the acceptor window intensity decay more closely. To do this, we performed simulations of the acceptor window fluorescence with experimental donor window and intrinsic fluorescence decay data as real inputs. Multi-exponential decay functions were simulated in MATLAB based on Equation 3, and these were convolved with the measured IRF of the TCSPC system. The decay rates and the total interacting fraction governing the simulated decay curves were based on measurements obtained in this study. Datasets were binned at 0.053 ns intervals and scaled to a maximum value of 5000 counts to reflect the experimental acceptor window measurements performed here. Poisson noise was added to each bin using the poissrnd() MATLAB function and the generated decays were fit to biexponential fluorescence decay models using the FLUOFIT iterative reconvolution package[44]. As with experimental TCSPC data, fits were rejected for $\chi^2_{\mathrm{R}} > 2$. Acceptor window fluorescence decays of the OG-GSH/GST-mCherry system were simulated for B values between 0.5 and 100 in increments of 0.5. Ten decay curves were produced for each value of B and analysed using a two-component nonlinear least squares fit, as applied to the experimental data. The parameters extracted from the least squares fits were then compared to those used to produce the decays.

In figure S14, it can be seen that the best-fit rise lifetime increased with B (reduced non-interacting donor bleed through) and consistently yielded a significantly lower value than the 1.33 ns time expected for an acceptor with a fluorescence lifetime longer than this value, a disagreement of 102(±1)% at $B(\Delta\lambda_A) = 9.7$. This is consistent with experimental observation. The corresponding absolute ratio of negative to positive amplitudes (as shown in figure S15) were also consistently lower than those input into Equation 3. At $B(\Delta\lambda_A) = 9.7$, the disagreement was 118(±1)%. In addition, the fluorescence decay lifetime was significantly

larger than that expected from a simple amplitude-weighted average of the positive amplitude components in equation 3 (figure S16), with a disagreement of 58(±1)% at $B(\Delta\lambda_A)=9.7$.

It was notable from the shape of the fluorescence decay in figure 4 that the turn over from a growth to decay in fluorescence was observed at a shorter time than the model acceptor fluorescence decay curves shown in figure S12. Indeed, plotting equation 3 for varying values of $B(\Delta\lambda_A)$ indicated that increased donor bleed through caused the turning point to shift to shorter times (figure S17). In our previous work investigating FRET between EGFP and mCherry, the acceptor window was characterised by $B(\Delta\lambda_A)$ value of 19.9. However, the present significantly smaller value of 9.7 arises from a greater fraction of the OG emission occurring in the acceptor window than that for EGFP ($q_D/q_A=0.07$ vs. 0.03) magnified by the larger quantum yield of OG (0.91 vs. 0.6)[2,4]. The presence of an increased donor bleed through signal containing no rise components will therefore shift the turning point of the acceptor window fluorescence to an earlier time than that of the intrinsic FRET signal. Thus, based on the computational simulations performed, the bleed through was skewing the rise lifetime to false shorter values to compensate for the apparently faster rise. This then had knock-on effects on the rise amplitude and decay lifetime, with parameters correlated in order to preserve a good fit ($\chi^2_R=1.7$) to the overall fluorescence decay[45].

In previous work, we demonstrated that the turning point of the acceptor window fluorescence decay data could be used to measure unknown FRET interaction parameters[46]. From differentiation of equation 3, the acceptor window fluorescence decay would be expected to turn over at a time t_0 given by the solution to,

$$\left[\begin{array}{l}\dfrac{F_{\mathrm{I}}\exp\left(-t_0/\tau_{\mathrm{D}}^{\mathrm{I}}\right)}{\tau_{\mathrm{D}}^{\mathrm{I}}}\\ +\dfrac{(1-F_{\mathrm{I}})\exp\left(-t_0/\tau_{\mathrm{D}}^{\mathrm{NI}}\right)}{\tau_{\mathrm{D}}^{\mathrm{NI}}}\end{array}\right]=Bf_1F_{\mathrm{I}}\left[\frac{\left(1/\tau_{\mathrm{D}}^{\mathrm{I}}\right)-\left(1/\tau_{\mathrm{D}}^{\mathrm{NI}}\right)}{\left(1/\tau_{\mathrm{D}}^{\mathrm{I}}\right)-\left(1/\tau_{\mathrm{A}}^{i=1}\right)}\right]\left[\begin{array}{l}\dfrac{\exp\left(-t_0/\tau_{\mathrm{D}}^{\mathrm{I}}\right)}{\tau_{\mathrm{D}}^{\mathrm{I}}}\\ -\dfrac{\exp\left(-t_0/\tau_{\mathrm{A}}^{i=1}\right)}{\tau_{\mathrm{A}}^{i=1}}\end{array}\right]$$
$$+B(1-f_1)F_{\mathrm{I}}\left[\frac{\left(1/\tau_{\mathrm{D}}^{\mathrm{I}}\right)-\left(1/\tau_{\mathrm{D}}^{\mathrm{NI}}\right)}{\left(1/\tau_{\mathrm{D}}^{\mathrm{I}}\right)-\left(1/\tau_{\mathrm{A}}^{i=2}\right)}\right]\left[\begin{array}{l}\dfrac{\exp\left(-t_0/\tau_{\mathrm{D}}^{\mathrm{I}}\right)}{\tau_{\mathrm{D}}^{\mathrm{I}}}\\ -\dfrac{\exp\left(-t_0/\tau_{\mathrm{A}}^{i=2}\right)}{\tau_{\mathrm{A}}^{i=2}}\end{array}\right] \qquad \text{(S45)}$$

where the fraction of total donors undergoing FRET to state 1 in GST-mC has been written as,

$$f = \frac{F_1^{\mathrm{I}}}{F_1^{\mathrm{I}} + F_2^{\mathrm{I}}} \tag{S46}$$

Experimentally, acceptor window fluorescence decays are best fit to a function of the form,

$$I(t) = A_{\mathrm{decay}} \exp\left(-t/\tau_{\mathrm{decay}}\right) - \left|A_{\mathrm{rise}}\right| \exp\left(-t/\tau_{\mathrm{rise}}\right) \tag{S47}$$

whose turning point t_0 is given by,

$$t_0 = \frac{\tau_{\mathrm{rise}}\tau_{\mathrm{decay}}}{\tau_{\mathrm{decay}} - \tau_{\mathrm{rise}}} \ln\left(\frac{\left|A_{\mathrm{rise}}\right|\tau_{\mathrm{decay}}}{A_{\mathrm{decay}}\tau_{\mathrm{rise}}}\right) \tag{S48}$$

Plotting the calculated turning points of the biexponential fits to the simulated data (equation S48) alongside the solution of equation S45 in figure S18 (here for $f = 0.5$), shows an excellent agreement between the turning point of the fits and the model used to generate the data, for all B values, in stark contrast to the disagreement between the individual extracted fit parameters and those expected from theory. Indeed, at $B = 9.7$, the values differed by only 4(±1)%, similar to the error of 3% expected from calculating the turning point of the fit using the parameters in figure 4. Thus, while each parameter of the biexponential fit to the acceptor window fluorescence intensity decay could not individually be correlated to the underlying energy transfer dynamics, close agreement with theory was achieved with a composite function containing each of the four parameters that, together, well characterise its shape, with χ_{R}^2 values of 1.6(±0.2) in the simulations and 1.7 for the experimental OG-GSH-GST-mC measurement (figure 4).

A linear dependence of the turning point on the proportion of FRET to each acceptor state for the theoretical model of FRET dynamics applied in this work (appendix S6) was demonstrated by numerically solving equation S45 for varying values of f using MATLAB, with a gradient of -0.1373(±0.0005) ns and y-intercept of 0.7504(±0.0003) ns (R^2=0.999). To investigate whether this relationship could be expected to hold for TCSPC data with a finite IRF, 50 simulated datasets were generated at each f value between 0 (all FRET to state 2)

and 1 (all FRET to state 1) at 0.01 intervals, using the established decay rates and total interacting fraction for the OG-GSH-GST-mCherry mixtures measured here. We found that the turning point of fits to the simulated TCSPC data, obtained using the biexponential fit parameters and equation S48, decreased linearly as the fraction of total donors interacting with acceptor state 1 was varied from 0 to 1, as shown in figure 5B. The presence of the IRF caused both the magnitude of the negative gradient and the y-intercept of the linear relationship to be larger than that of the theoretical solution, at -0.1540(±0.0005) ns and 0.7157(±0.0003) ns (R^2=0.999).

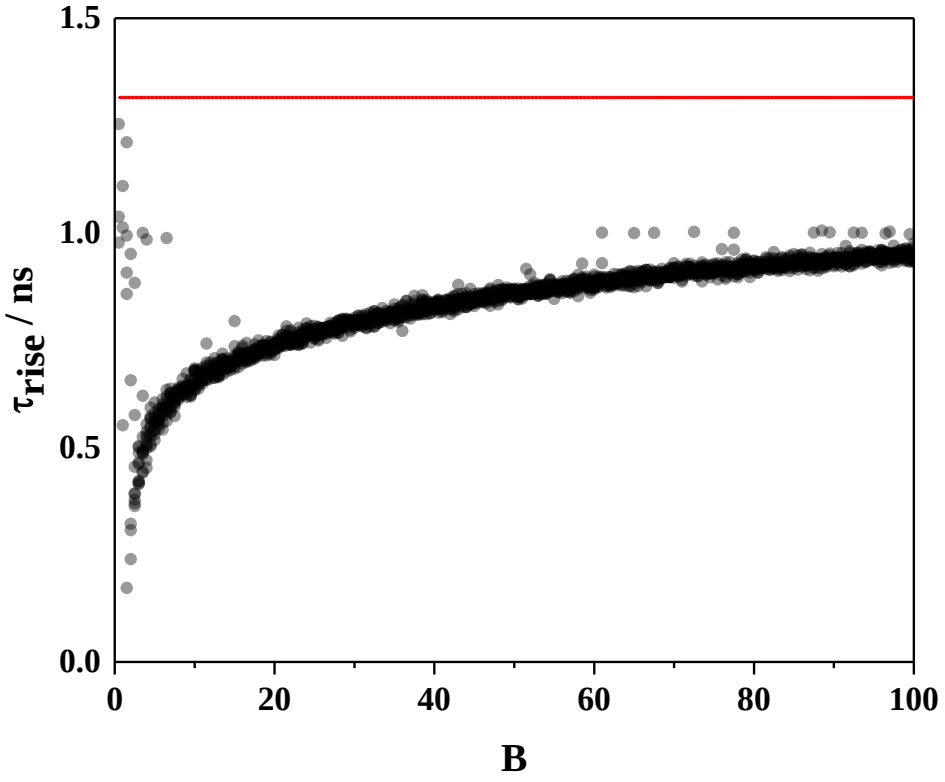

Figure S14: Variation in rise lifetime extracted from simulated fluorescence decays at increasing values of B (decreasing donor bleed through). Values were systematically lower than either of the negative amplitude lifetimes expected from equation 3 of 1.315 ns (short lifetime in GST-mCherry, negative transfer amplitude to acceptor state 1) or 1.33 ns (interacting donor lifetime, positive transfer amplitude to acceptor state 2), and lifetimes decreased dramatically for $B < 10$. The functional form of this variation is therefore more complex than simply the amplitude-weighted average of these two lifetimes (1.32 ns, red line) with a discrepancy between data and theory, averaged across the range of B values, of 60(±30)% (mean±S.D.).

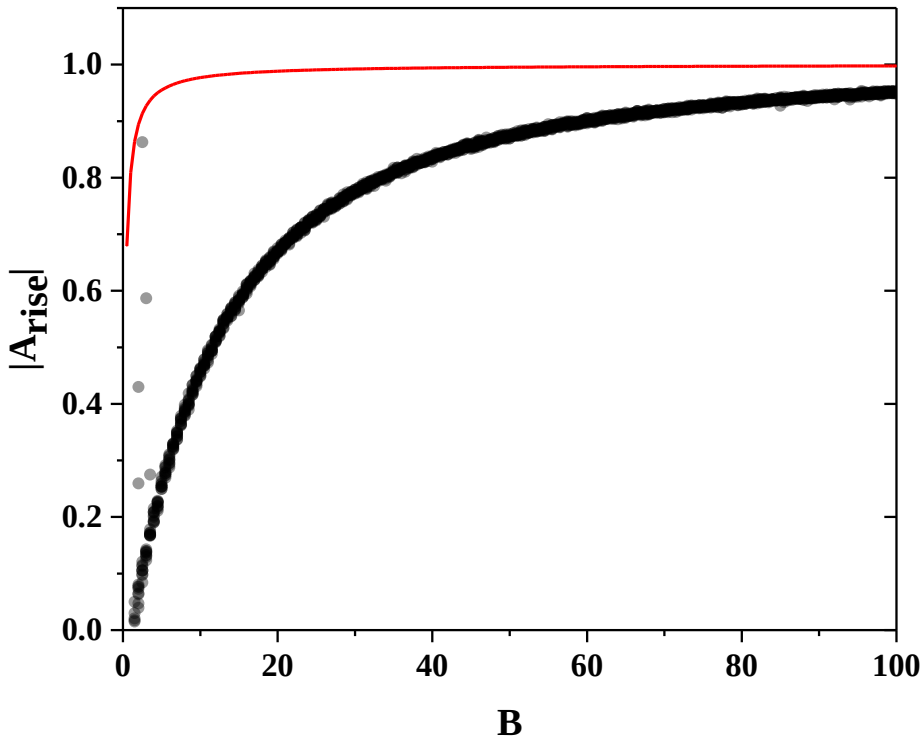

Figure S15: Variation in rise amplitude extracted from simulated fluorescence decays at increasing values of B. In the presence of donor bleed through, the best-fit amplitude was significantly smaller than that expected from a ratio of the negative amplitude components to the positive amplitude components present in equation 3 (red line), with a discrepancy averaged across the range of B values of 70(±300)%.

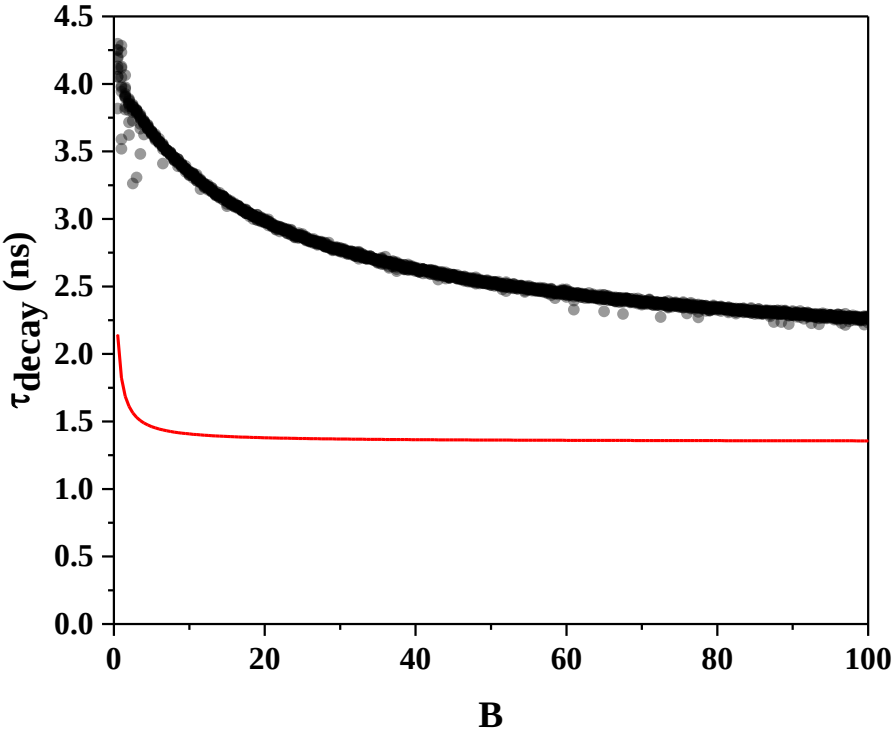

Figure S16: Variation in decay lifetime extracted from simulated fluorescence decays at increasing values of B. For all B, an amplitude-weighted average of the positive amplitude components in equation 3 (red line) did not describe the lifetimes extracted from the fits, with a discrepancy averaged across the range of B values of 47(±6)%.

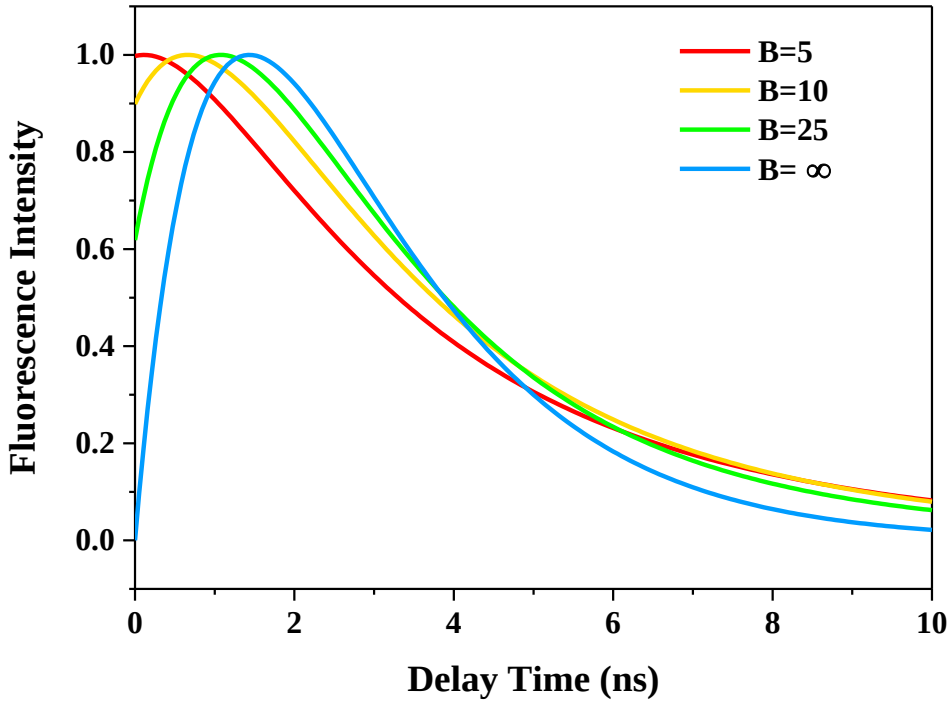

Figure S17: Time-resolved acceptor window fluorescence decay curves with varying levels of donor bleed through, calculated using equation 3. Increased bleed through (decreased B) shifts the turning point of the curve to shorter delay times.

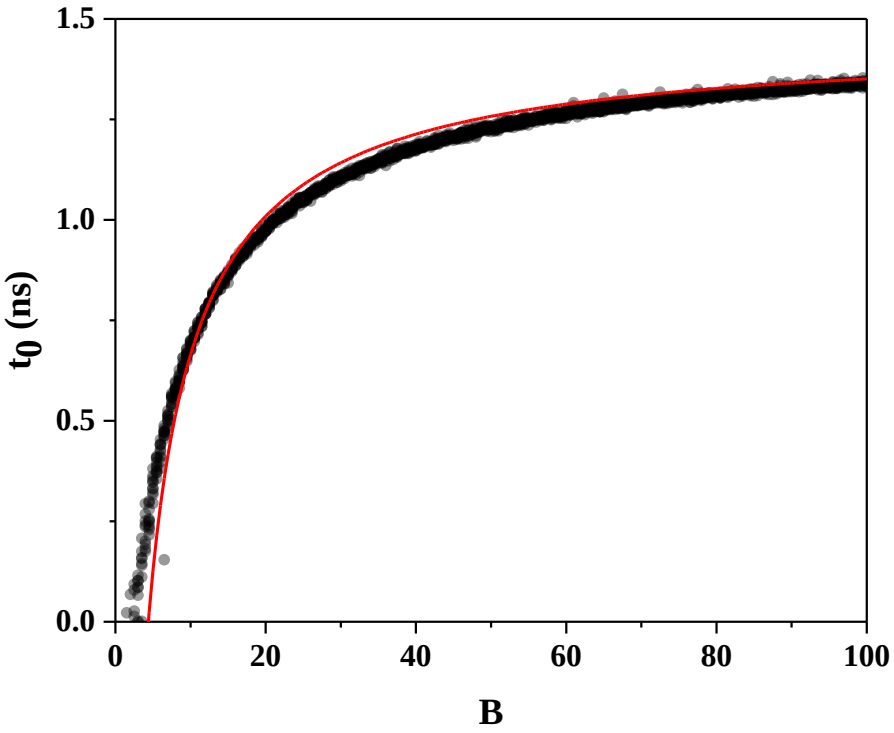

Figure S18: Comparison of turnover points extracted from simulated fluorescence decays (black data points, equation S48) with those expected from theory (red line, equation S45) for increasing values of B. At all levels of donor bleed through, theory and fits showed close agreement. At $B = 9.7$, as is the case for the acceptor window in the OG-GSH GST-mC experiments performed here, the discrepancy was only 4(±1)%, similar to the experimental error in the determination of the turning point.

Appendix S12: Acceptor window anisotropy decay analysis

If the acceptor in a FRET pair is oriented at a fixed angle of θ_{DA} relative to the donor, its fluorescence anisotropy upon donor excitation will be depolarised by a factor[47],

$$d_A^I = \frac{3\cos^2\theta_{DA} - 1}{2} \tag{S49}$$

Thus, if the assumption of a fixed transition dipole angle holds, such as if donor and acceptor diffusion take place at a much slower time scale than FRET, the associated anisotropy model describing the acceptor window anisotropy decay, with $I_{total}(t)$ given by equation 3, would be,

$$R_{measured}(t) = \frac{I_{donor}(t)R_{donor}(t) + I_{acceptor}(t)R_{acceptor}(t)}{I_{total}(t)} \tag{S50}$$

$$I_{donor}(t)R_{donor}(t) = R(0)\begin{bmatrix} \eta_{free}(1-F_I)\exp(-t/\tau_D^{NI})\exp(-t/\tau_{free}) \\ +F_I\exp(-t/\tau_D^I)[A\exp(-t/\tau_{fast})+(1-A)\exp(-t/\tau_{slow})] \\ +(1-\eta_{free})(1-F_I)\exp(-t/\tau_D^{NI})[A\exp(-t/\tau_{fast})+(1-A)\exp(-t/\tau \end{bmatrix} \tag{S51}$$

$$I_{acceptor}(t) = BF_I\left\{X_1\left[\exp(-t/\tau_A^{i=1}) - \exp(-t/\tau_D^I)\right] + X_2\left[\exp(-t/\tau_A^{i=2}) - \exp(-t/\tau_D^I)\right]\right\} \tag{S52}$$

$$R_{acceptor}(t) = R(0)d_A^I[a\exp(-t/\tau_1) + (1-a)\exp(-t/\tau_2)] \tag{S53}$$

As seen in figure 6A, the assumption that the donor and acceptor remain at a fixed θ_{DA} angle on the time scales over which FRET occurs did not hold in the OG-GSH-GST-mCherry system based on the poor fit of equation S50 to the experimental data. In order to qualitatively compare the acceptor anisotropy measurements with the analytical model of fluorescence anisotropy decay in the presence of FRET, we took advantage of our knowledge of the intensity weightings in the measured associated anisotropies to recover the acceptor anisotropy decay from the donor bleed through contribution. This was achieved by rearranging equation S50 to give,

$$R_{\text{acceptor}}(t) = \frac{I_{\text{total}}(t)}{I_{\text{acceptor}}(t)} R_{\text{measured}}(t) - \frac{I_{\text{donor}}(t)}{I_{\text{acceptor}}(t)} R_{\text{donor}}(t) \qquad \text{(S54)}$$

A triexponential decay function was arbitrarily fit ($\chi_R^2 = 1.1$) to the measured acceptor window anisotropy data in order to obtain a "noise-free" description of $R_{\text{measured}}(t)$. This allowed the two terms in equation S54 to be calculated using the functional forms of the intensity decays and the donor window anisotropy, with all parameters provided by the results obtained in this work. These are plotted in figure S19. The intensity-weighted subtraction in equation S54 was performed both on the noiseless $R_{\text{measured}}(t)$ curve drawn through the datapoints and directly on the $R_{\text{measured}}(t)$ dataset. The results of both of these calculations are shown in figure 6B.

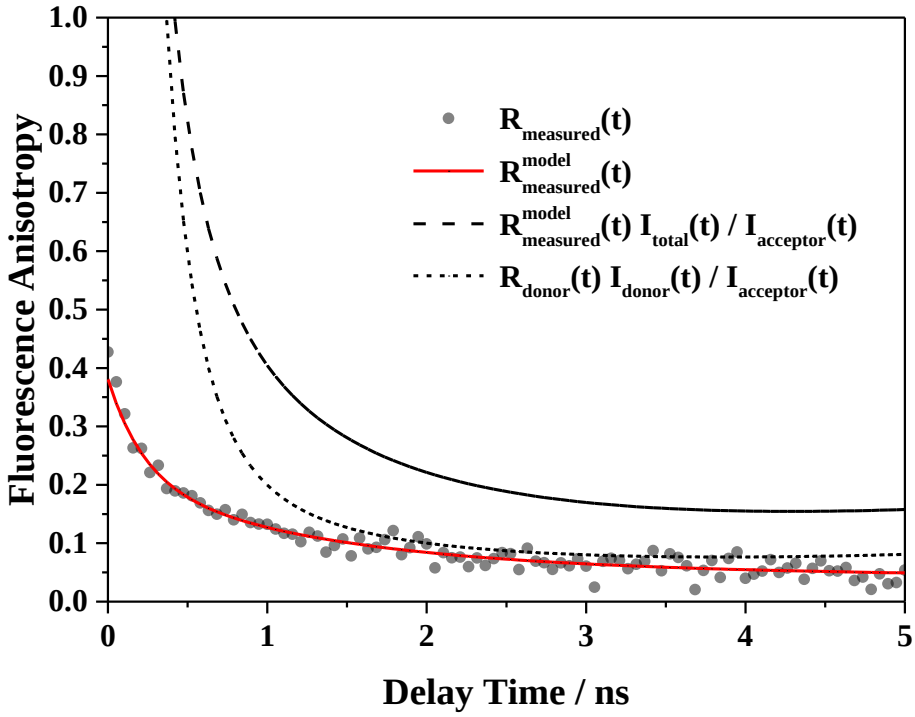

Figure S19: Acceptor window fluorescence anisotropy decay of OG-GSH GST-mC mixture. In order to qualitatively understand the orientational dynamics of the FRET interaction, the intensity-weighted anisotropy contribution of the donor bleed through was subtracted from the measured data using equation S54. The two terms involved in this operation are plotted using a triexponential model arbitrarily fit to the experimental data ($\chi^2_R = 1.1$) as the $R_{measured}(t)$ in order to reduce the influence of noise.

Supporting References

(1) Shaner, N. C.; Campbell, R. E.; Steinbach, P. A.; Giepmans, B. N. G.; Palmer, A. E.; Tsien, R. Y. Improved Monomeric Red, Orange and Yellow Fluorescent Proteins Derived from Discosoma Sp. Red Fluorescent Protein. *Nat. Biotechnol.* **2004**, *22* (12), 1567–1572.

(2) Rusinova, E.; Tretyachenko-Ladokhina, V.; Vele, O. E.; Senear, D. F.; Alexander Ross, J. B. Alexa and Oregon Green Dyes as Fluorescence Anisotropy Probes for Measuring Protein–protein and Protein–nucleic Acid Interactions. *Anal. Biochem.* **2002**, *308* (1), 18–25.

(3) Magde, D.; Wong, R.; Seybold, P. G. Fluorescence Quantum Yields and Their Relation to Lifetimes of Rhodamine 6G and Fluorescein in Nine Solvents: Improved Absolute Standards for Quantum Yields. *Photochem. Photobiol.* **2002**, *75* (4), 327–334.

(4) Masters, T. A.; Marsh, R. J.; Armoogum, D. A.; Nicolaou, N.; Larijani, B. B.; Bain, A. J. Restricted State Selection in Fluorescent Protein Forster Resonance Energy Transfer. *J. Am. Chem. Soc.* **2013**, *135* (21), 7883–7890.

(5) Xu, C.; Webb, W. W. Measurement of Two-Photon Excitation Cross Sections of Molecular Fluorophores with Data from 690 to 1050 Nm. *J. Opt. Soc. Am. B* **1996**, *13* (3), 481–491.

(6) Beaumont, P. C.; Johnson, D. G.; Parsons, B. J. Photophysical Properties of Laser Dyes: Picosecond Laser Flash Photolysis Studies of Rhodamine 6G, Rhodamine B and Rhodamine 101. *J. Chem. Soc. Faraday Trans.* **1993**, *89* (23), 4185.

(7) Drobizhev, M.; Tillo, S.; Makarov, N. S.; Hughes, T. E.; Rebane, A. Absolute Two-Photon Absorption Spectra and Two-Photon Brightness of Orange and Red Fluorescent Proteins. *J. Phys. Chem. B* **2009**, *113* (4), 855–859.

(8) Drobizhev, M.; Makarov, N. S.; Tillo, S. E.; Hughes, T. E.; Rebane, A. Two-Photon Absorption Properties of Fluorescent Proteins. *Nat Meth 8* (5), 393–399.

(9) Blacker, T. S.; Marsh, R. J.; Duchen, M. R.; Bain, A. J. Activated Barrier Crossing Dynamics in the Non-Radiative Decay of NADH and NADPH. *Chem. Phys.* **2013**, *422*, 184–194.

(10) Kapusta, P.; Erdmann, R.; Ortmann, U.; Wahl, M. Time-Resolved Fluorescence Anisotropy Measurements Made Simple. *J. Fluoresc.* **2003**, *13* (2), 179–183.

(11) Bain, A. J.; Chandna, P.; Bryant, J. Picosecond Polarized Fluorescence Studies of Anisotropic Fluid Media. I. Theory. *J. Chem. Phys.* **2000**, *112* (23), 10418–10434.

(12) Lipari, G.; Szabo, A. Effect of Librational Motion on Fluorescence Depolarization and Nuclear Magnetic Resonance Relaxation in Macromolecules and Membranes. *Biophys. J.* **1980**, *30* (3), 489–506.

(13) Tao, T. Time-Dependent Fluorescence Depolarization and Brownian Rotational Diffusion Coefficients of Macromolecules. *Biopolymers* **1969**, *8* (5), 609–632.

(14) Chuang, T. J.; Eisenthal, K. B. Studies of Effects of Hydrogen Bonding on Orientational Relaxation Using Picosecond Light Pulses. *Chem. Phys. Lett.* **1971**, *11* (3), 368–370.

(15) Gumy, J.-C.; Vauthey, E. Picosecond Polarization Grating Study of the Effect of Excess Excitation Energy on the Rotational Dynamics of Rhodamine 6G in Different Electronic States. *J. Phys. Chem.* **1996**, *100* (21), 8628–8632.

(16) Bain, A. J.; Chandna, P.; Butcher, G.; Bryant, J. Picosecond Polarized Fluorescence Studies of Anisotropic Fluid Media. II. Experimental Studies of Molecular Order and Motion in Jet Aligned Rhodamine 6G and Resorufin Solutions. *J. Chem. Phys.* **2000**, *112* (23), 10435.

(17) Chadborn, N.; Bryant, J.; Bain, A. J.; O'Shea, P. Ligand-Dependent Conformational Equilibria of Serum Albumin Revealed by Tryptophan Fluorescence Quenching. *Biophys J* **1999**, *76* (4), 2198–2207.

(18) Kinosita, K.; Kawato, S.; Ikegami, A. A Theory of Fluorescence Polarization Decay in Membranes. *Biophys. J.* **1977**, *20* (3), 289–305.

(19) Ko, C. W.; Wei, Z.; Marsh, R. J.; Armoogum, D. A.; Nicolaou, N.; Bain, A. J.; Zhou, A.; Ying, L. Probing Nanosecond Motions of Plasminogen Activator Inhibitor-1 by Time-Resolved Fluorescence Anisotropy. *Mol. Biosyst.* **2009**, *5* (9), 1025–1031.

(20) Díaz, F. G.; García de la Torre, J. Simulation of the Rotational Brownian Dynamics of a Simple, Segmentally Flexible Model: The Elastic Trumbbell. *J. Chem. Phys.* **1988**, *88* (12), 7698.

(21) Kursula, I.; Heape, A. M.; Kursula, P. Crystal Structure of Non-Fused Glutathione S-Transferase from Schistosoma Japonicum in Complex with Glutathione. *Protein Pept. Lett.* **2005**, *12* (7), 709–712.

(22) Reddington, S. .; Driezis, S.; Hartley, A. .; Watson, P. .; Rizkallah, P. .; Jones, D. D. Genetically Encoded Phenyl Azide Photochemistry Drive Positive and Negative Functional Modulation of a Red Fluorescent Protein. *Rsc Adv* **2015**.

(23) Wahl, P. Analysis of Fluorescence Anisotropy Decays by a Least Square Method. *Biophys. Chem.* **1979**, *10* (1), 91–104.

(24) Alper, J. S.; Gelb, R. I. Standard Errors and Confidence Intervals in Nonlinear Regression: Comparison of Monte Carlo and Parametric Statistics. *J. Phys. Chem.* **1990**, *94* (11), 4747–4751.

(25) Bain, A. J. Multiphoton Processes. In *Photonics*; John Wiley & Sons, Inc., 2015; pp 279–320.

(26) Bucci, E.; Steiner, R. F. Anisotropy Decay of Fluorescence as an Experimental Approach to Protein Dynamics. *Biophys. Chem.* **1988**, *30* (3), 199–224.

(27) Ortega, A.; Amorós, D.; García de la Torre, J. Prediction of Hydrodynamic and Other Solution Properties of Rigid Proteins from Atomic- and Residue-Level Models. *Biophys. J.* **2011**, *101* (4), 892–898.

(28) Harvey, S. C.; Cheung, H. C. Transport Properties of Particles with Segmental Flexibility. II. Decay of Fluorescence Polarization Anisotropy from Hinged Macromolecules. *Biopolymers* **1980**, *19* (4), 913–930.

(29) Garcia de la Torre, J.; Perez Sanchez, H. E.; Ortega, A.; Hernandez, J. G.; Fernandes, M. X.; Diaz, F. G.; Lopez Martinez, M. C. Calculation of the Solution Properties of Flexible Macromolecules: Methods and Applications. *Eur. Biophys. J.* **2003**, *32* (5), 477–486.

(30) Chen, W.; Avezov, E.; Schlachter, S. C.; Gielen, F.; Laine, R. F.; Harding, H. P.; Hollfelder, F.; Ron, D.; Kaminski, C. F. A Method to Quantify FRET Stoichiometry with Phasor Plot Analysis and Acceptor Lifetime Ingrowth. *Biophys. J.* **2015**, *108* (5), 999–1002.

(31) Ainavarapu, S. R. K.; Brujic, J.; Huang, H. H.; Wiita, A. P.; Lu, H.; Li, L.; Walther, K. A.; Carrion-Vazquez, M.; Li, H.; Fernandez, J. M. Contour Length and Refolding Rate of a Small Protein Controlled by Engineered Disulfide Bonds. *Biophys. J.* **2007**, *92* (1), 225–233.

(32) Harvey, S. C.; Mellado, P.; Torre, J. G. de la. Hydrodynamic Resistance and Diffusion Coefficients of Segmentally Flexible Macromolecules with Two Subunits. *J. Chem. Phys.* **1983**, *78* (4), 2081.

(33) Hassager, O. Kinetic Theory and Rheology of Bead-Rod Models for Macromolecular Solutions. I. Equilibrium and Steady Flow Properties. *J. Chem. Phys.* **1974**, *60* (5), 2111.

(34) Nagasaka, K.; Yamakawa, H. Dynamics of Weakly Bending Rods: A Trumbbell Model. *J. Chem. Phys.* **1985**, *83* (12), 6480.

(35) Roitman, D. B.; Zimm, B. H. An Elastic Hinge Model for Dynamics of Stiff Chains. I. Viscoelastic Properties. *J. Chem. Phys.* **1984**, *81* (12), 6333.

(36) Roitman, D. B.; Zimm, B. H. An Elastic Hinge Model for Dynamics of Stiff Chains. II. Transient Electro-Optical Properties. *J. Chem. Phys.* **1984**, *81* (12), 6348.

(37) Roitman, D. B. An Elastic Hinge Model for Dynamics of Stiff Chains. III. Viscoelastic and Kerr-Effect Behavior of Bent Molecules. *J. Chem. Phys.* **1984**, *81* (12), 6356.

(38) Lipari, G.; Szabo, A. Effect of Librational Motion on Fluorescence Depolarization and Nuclear Magnetic Resonance Relaxation in Macromolecules and Membranes. *Biophys. J.* **1980**, *30* (3), 489–506.

(39) Armstrong, R. N. Glutathione S-Transferases: Reaction Mechanism, Structure, and Function. *Chem. Res. Toxicol.* **1991**, *4* (2), 131–140.

(40) Valeur, B.; Berberan-Santos, M. N. *Molecular Fluorescence Principles and Applications*; Wiley-VCH, 2013.

(41) Tanaka, F.; Mataga, N. Dynamic Depolarization of Interacting Fluorophores. Effect of Internal Rotation and Energy Transfer. *Biophys. J.* **1982**, *39* (2), 129–140.

(42) Tanaka, F. Effects of Internal Rotations on the Time-Resolved Fluorescence in a Bichromophoric Protein System Under the Energy Transfer Interaction. *J. Fluoresc.* *10* (1), 13–20.

(43) Tanaka, F. Theory of Time-Resolved Fluorescence under the Interaction of Energy Transfer in a Bichromophoric System: Effect of Internal Rotations of Energy Donor and Acceptor. *J. Chem. Phys.* **1998**, *109* (3), 1084.

(44) Enderlein, J.; Erdmann, R. Fast Fitting of Multi-Exponential Decay Curves. *Opt. Commun.* **1997**, *134* (1-6), 371–378.

(45) Grinvald, A.; Steinberg, I. Z. On the Analysis of Fluorescence Decay Kinetics by the Method of Least-Squares. *Anal. Biochem.* **1974**, *59* (2), 583–598.

(46) Blacker, T. S.; Duchen, M. R.; Bain, A. J. Heterogeneity and Restricted State Selection in FRET with Fluorescent Proteins; International Society for Optics and Photonics, 2016; p 971401.

(47) Dale, R. E.; Eisinger, J.; Blumberg, W. E. The Orientational Freedom of Molecular Probes. The Orientation Factor in Intramolecular Energy Transfer. *Biophys. J.* **1979**, *26* (2), 161–193.